

1 **Understanding the molecular mechanism of umami recognition by** 2 **T1R1-T1R3 using molecular dynamics simulations**

3 Hai Liu^{1, 𠄎}, Lin-Tai Da^{2, 𠄎*}, Yuan Liu^{3*}

4 **1** College of Food Sciences & Technology, Shanghai Ocean University, Shanghai, China, **2** Key
5 Laboratory of Systems Biomedicine (Ministry of Education), Shanghai Center for Systems
6 Biomedicine, Shanghai Jiao Tong University, Shanghai, China, **3** Department of Food Science
7 & Technology, School of Agriculture and Biology, Shanghai Jiao Tong University, Shanghai,
8 China

9 𠄎 These authors contributed equally to this work.

10 * Corresponding author

11 E-mail: darlt@sjtu.edu.cn; y_liu@sjtu.edu.cn

12

13 Funding: This work was funded by the National Natural Science Foundation of China (Grant
14 No. 31622042, 31371790, 31271900).

15

16 **Abstract**

17 Taste receptor T1R1-T1R3 can be activated by binding to several natural ligands, e.g., L-
18 glutamate and 5'-ribonucleotides etc., thereby stimulating the umami taste. The molecular
19 mechanism of umami recognition at an atomic level, however, remains elusive. Here, using
20 homology modeling, molecular docking and molecular dynamics (MD) simulations, we
21 investigate the effects of five natural umami ligands on the structural dynamics of T1R1-T1R3.
22 Our work identifies the key residues that are directly involved in recognizing the binding

23 ligands. In addition, two adjacent binding sites in T1R1 are determined for substrate binding,
24 and depending on the molecular size and chemical properties of the incoming ligand, one or
25 both these binding sites can be occupied. More interestingly, the binding of varied ligands can
26 lead to either closing or opening of T1R1, based on which, we further classify the five ligands
27 into two groups. This different binding effects are likely associated with the distinct umami
28 signals stimulated by various ligands. This work warrants new experimental assays to further
29 validate the theoretical model and provides guidance to design more effective umami ligands.
30

31 **Author summary**

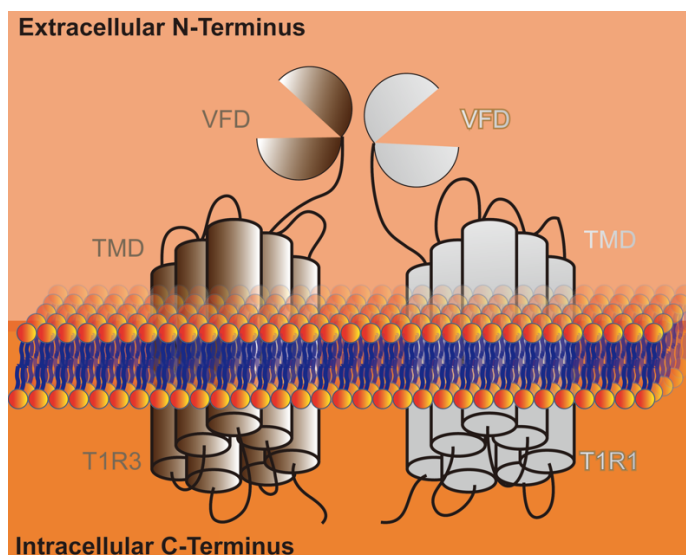
32 Umami, as the fifth basic taste, is induced by umami substances from the natural food, such
33 as L-glutamate, 5'-ribonucleotides, and peptides etc. These umami substances are widely
34 added to foods as flavor enhancers to promote food quality. However, although extensive
35 experimental and theoretical studies have been devoted to revealing the recognition
36 mechanisms of the taste receptor T1R1-T1R3 to the umami ligands, the detailed molecular
37 mechanism is still unknown, largely due to the lack of the receptor structure. Here, using a
38 new template structure different from the former theoretical studies, we constructed a more
39 accurate homology model of T1R1-T1R3. Based on this receptor model, combined with
40 molecular docking and MD simulations, we investigate how different ligands with varied
41 molecular size and chemical groups might affect the dynamics of T1R1. Our work provides the
42 structural basis for relating the dynamics of umami receptor induced by varied ligands to the
43 resulting umami signal.

44

45 **Introduction**

46 The umami, induced by binding of L-glutamic acid salt (MSG) to its taste receptor type 1 (T1R),
47 was discovered as one of the five basic tastes by Ikeda in 1908 [1-3]. T1R is comprised of three
48 members, including T1R1, T1R2, and T1R3, which can further dimerize to form either sweet
49 taste receptor (T1R2-T1R3) or umami taste receptor (T1R1-T1R3) [2, 4]. T1R belongs to the G-
50 protein-coupled receptors (GPCRs) family and is assigned to the same class as the
51 metabotropic glutamate receptor (mGluR) by previous phylogenetic tree analysis [5].

52 Human T1R1-T1R3 (hT1R1-T1R3) consists of a large extracellular N-Venus Flytrap domain
53 (VFD), and a seven-transmembrane domain (TMD), connected by a small cysteine-rich
54 domain (CRD) (Fig 1) [5]. VFD has been determined to be the ligand binding domain by former
55 site-directed mutagenesis studies using chimeric T1R constructs based on human sweet and
56 umami T1R VFD domains [3, 6], or human and rat T1R VFD domains [7-9]. Notably, apart from
57 VFD, the hT1R1 TMD is also considered as a potential substrate binding site for some umami
58 substances, such as methional [10], and S807 [6]. As a result, the T1R TMD couples with a G
59 protein inside the cell to stimulate the umami signal [11]. More interestingly, the umami can
60 be further enhanced by binding to additional 5'-ribonucleotides, such as disodium 5'-
61 guanylate (GMP) and disodium 5'-inosinate (IMP) [2, 4, 12]. This synergistic enhancement is
62 considered to be the most unique sensory feature of umami compared to other four basic
63 tastes. Notably, in addition to L-Glu, Nelson et al. and Toda et al. found that the hT1R1-T1R3
64 can also be activated by other standard L-amino acids, whereas hT1R1 are more sensitive to
65 L-Glu compared to other amino acids [2, 8]. Moreover, small peptides, especially those with
66 a molecular weight lower than 3000 Daltons, can also stimulate umami [13-15].



67

68 **Fig 1.** Schematic illustration of T1R1-T1R3 structure, which is a heterodimer with each subunit composed
69 of one TMD and one VFD connected by CRD.

70 To date, the crystal structure of hT1R1-T1R3 VFD has not been resolved. Computational
71 modeling has been used to construct a homology model of hT1R1-T1R3 and to understand
72 the molecular mechanism of umami recognition. For example, Cascales et al. [16] constructed
73 an hT1R1-T1R3 VFD model using the mGluR1 structure (PDB id: 1EWK) as a template. Their
74 MD simulations reveal that the L-Glu tends to induce the closing of T1R1 but not for T1R3.
75 Likewise, Dang et al. [17] also found that the T1R1 can undergo closing/opening motions in
76 the presence of umami peptides. In addition, Yu et al. [15] constructed a three-dimensional
77 quantitative structure-activity relationship model for five peptides and their umami
78 intensities. Moreover, Dang et al. [18] studied the molecular mechanism of the synergistic
79 effect between L-Glu and umami peptide using molecular docking. They revealed that after
80 T1R1 binds to MSG, T1R3 can adopt an open state that can recruit the peptides, therefore,
81 leading to the synergistic effect on promoting the umami intensity. In sharp contrast, Zhang
82 et al. [7] found that IMP and L-Glu can bind to hT1R1-VFD simultaneously, which provides
83 another explanation for the synergy. In addition, they further identified eight residues that
84 are critical for ligand binding using site-directed mutagenesis. Taken together, the previous

85 theoretical studies have provided some structural basis for the ligand-bound hT1R1-T1R3
86 complexes. However, the effects of ligand binding on the dynamics of hT1R1-T1R3 are largely
87 unknown, and how structurally varied ligands might affect the dynamics of hT1R1-T1R3 in
88 different manners are also unclear. Moreover, the homology template used in former work
89 is mGluR, which has lower sequence identity (< 30 %) with hT1R1 or hT1R3 compared to the
90 recently obtained crystal structure of fish T1R2a-T1R3 [19].

91 Here, by employing homology modeling, molecular docking, and MD simulations, we
92 constructed five ligand-bound hT1R1-T1R3 VFD complexes based on the fish T1R2a-T1R3
93 structure (PDB id: 5X2M), including MSG, WSA (sodium succinate), GMP, IMP, and BMP (beefy
94 meaty peptide). We find all the ligands can reach into a cleft region of hT1R1-VFD, and more
95 interestingly, two binding sites in hT1R1-VFD are identified. Depending on the molecular size
96 and carried charges of the incoming ligands, one or both of the above two sites can be
97 occupied. Moreover, based on the effects of ligand binding on the closing and opening
98 motions of hT1R1-VFD, we further classify the ligands into two groups, which may relate to
99 their different bioactivities as umami substances. Our findings provide an atomistic-level
100 understanding of the structure-function relationship for different substrates, which further
101 guides to design more structurally diversified umami ligands.

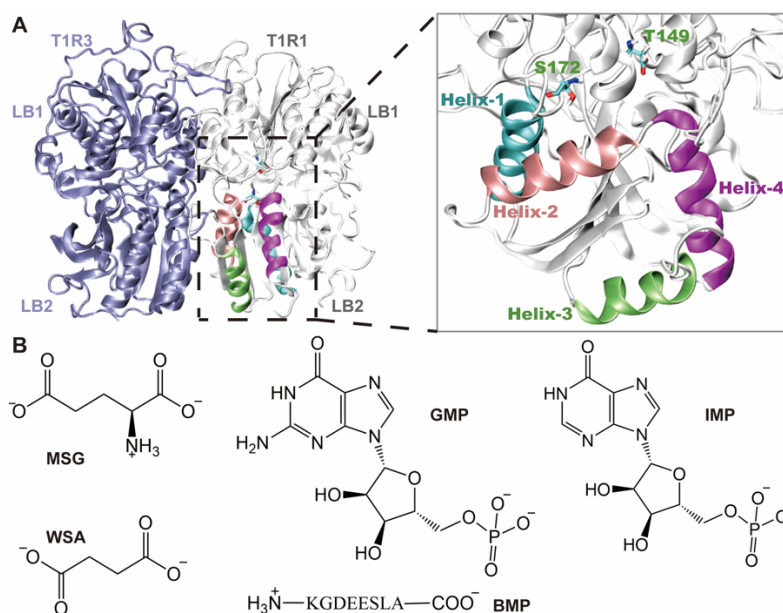
102

103 **Results**

104 **Structural features of hT1R1-T1R3 VFD in complex with different umami ligands.**

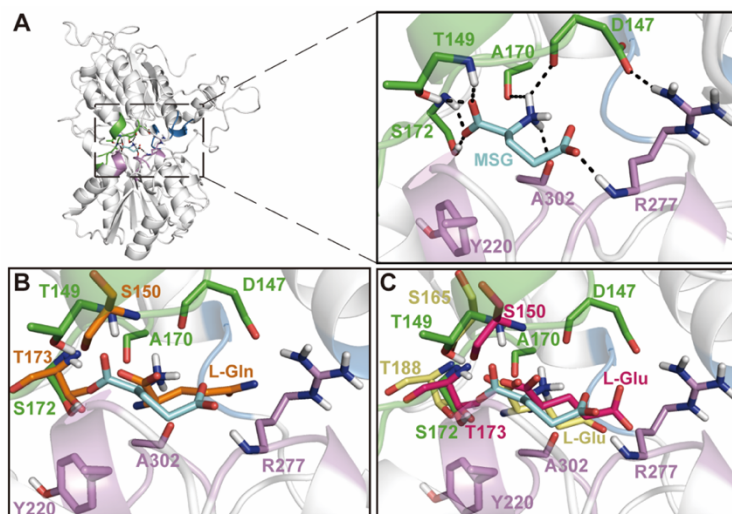
105 A homology model of hT1R1-T1R3 VFD was constructed based on the counterpart domain
106 from fish sweet receptor T1R2a-T1R3 (PDB id: 5X2M) complexed with one L-glutamine (L-Gln)
107 ligand. The hT1R1-VFD and hT1R3-VFD subunits share sequence identity of 33.03 % and 33.87

108 % with the corresponding subunit of fish sweet receptor, respectively, which is higher than
109 mGluR that was used in former studies [3, 8, 17]. Moreover, we constructed the phylogenetic
110 tree for T1R and mGluR based on their VFD, sourced from human, fish, mouse, and rat (S2
111 Fig). The results show that the hT1R1-T1R3 VFD has higher homology with fish T1R2a-T1R3
112 compared to mGluR1, indicating that fish T1R2a-T1R3 is a better homology template to
113 construct the hT1R1-T1R3 VFD structure. As shown in Fig 2A, hT1R1-T1R3 VFD is a
114 heterodimer, consisting of two ligand binding (LB) domains that form pseudo-symmetrical
115 lobes, and each LB domain is comprised of two parts, LB1 and LB2, resembling to the
116 structural characteristics of mGluR1 and human GABA(B) receptor [19-21].



118 **Fig 2.** The constructed model of hT1R1-T1R3 VFD and chemical formulas of five umami ligands. **(A)**
119 Homology model of hT1R1-T1R3 VFD, in which hT1R1 and hT1R3 are shown in gray and blue cartoons,
120 respectively. The ligand binding site and key structural motifs of hT1R1 are highlighted in the zoom-in image,
121 in which two active site residues S172 and T149 are shown in cyan sticks, and four LB2 helices, including
122 the residues 192-205 (helix-1), 219-232 (helix-2), 256-266 (helix-3), and 277-290 (helix-4), are highlighted
123 in cyan, pink, lime, and magenta, respectively. **(B)** Chemical structures of five umami ligands studied here,
124 including MSG, WSA, GMP, IMP, and BMP.

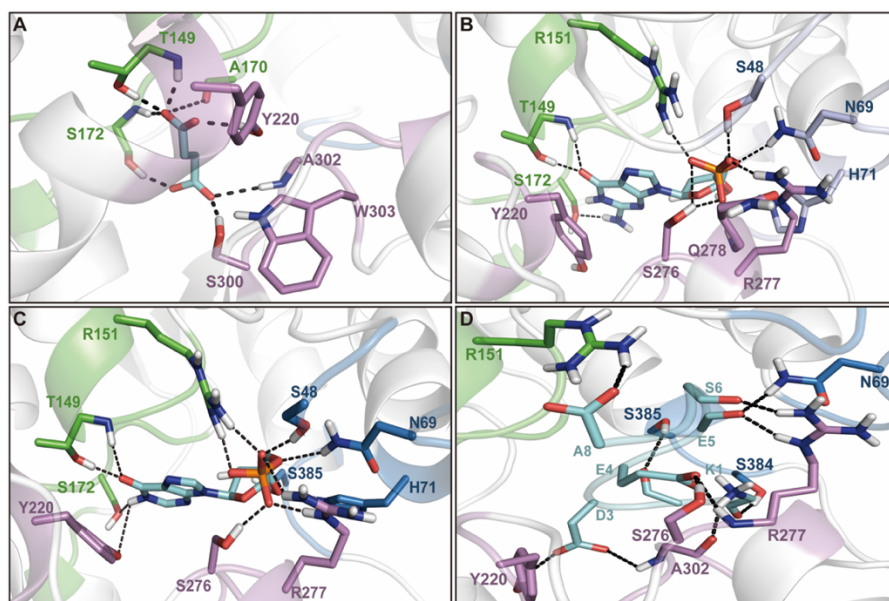
125 Based on the modeled structure of ht1R1-T1R3 VFD, we further constructed ligand-bound
126 ht1R1-T1R3 VFD complexes for five natural umami ligands using molecular docking strategies,
127 including MSG, WSA, GMP, IMP, and BMP (Fig 2B). Only ht1R1 was used as the docking
128 receptor since ht1R3 was found to play an auxiliary role for ligand binding [8, 22]. For each
129 ligand, the structure with the highest binding affinity was used as the final docking complex
130 for the following analysis. In the MSG-bound complex, the ligand can sit in a cleft region
131 formed by LB1 and LB2, and forms direct contacts with the residues S172, T149, A170, D147,
132 A302, R277, and Y200 (Fig 3A). In specific, MSG is sandwiched between the side-chains of
133 D147 and Y220, and forms hydrogen bonds (HBs) with S172 and T149 through its C_α-COO⁻
134 group (Figs 2A and 3A). In addition, the C_α-NH₃⁺ terminus of MSG can form HBs with the main
135 chain of A170, D147, and A302. The side-chain carboxylate group of MSG can establish one
136 HB with the R277 amide.



137
138 **Fig 3. (A)** Docking complex of MSG-bound ht1R1-VFD. The detailed interactions between MSG and nearby
139 residues are highlighted in the zoom-in image, MSG is shown in cyan sticks and the ht1R1-VFD residues
140 are shown in green/blue/violet sticks. Several key HBs are highlighted with black dashed lines. **(B)** Structural
141 overlay of the MSG-bound ht1R1-VFD to fish T1R2a-T1R3 (PDB id: 5X2M, ligand: L-Gln), and the ligand L-
142 Gln, S150, and T173 in T1R2a-T1R3 are shown in orange sticks. **(C)** Structural overlay of the MSG-bound

143 hT1R1-VFD complex to fish T1R2a-T1R3 (PDB id: 5X2P, ligand: L-Glu) and mGluR1 (PDB id: 1EWK, ligand: L-
144 Glu). L-Glu, S150, and T173 in T1R2a-T1R3 are shown in hot-pink sticks; L-Glu, S165, and T188 in mGluR1
145 are shown in pale-yellow sticks.

146 To evaluate the docking result, we compared the MSG-bound hT1R1-T1R3 VFD complex
147 with the crystal structure of fish T1R2a-T1R3 (PDB id: 5X2M, 5X2P) and mGluR1 (PDB id: 1EWK)
148 where the binding ligand is either L-Gln (from 5X2M) or L-Glu (from 5X2P, 1EWK) [19, 20], so
149 that we can compare the ligand binding modes for different complexes. We firstly
150 superimposed our modeled hT1R1-T1R3 VFD to each of the above three crystal structures by
151 their C_α atoms. Notably, the C_α-COO⁻ group of ligands from the four complexes all reside in a
152 same pocket and lie in a similar orientation (Fig 3B and 3C). However, it is worth to note that
153 since the active site residues for different systems are not fully conserved among different
154 systems, the detailed interaction networks between the ligand and nearby residues are also
155 different (S1 Fig). For example, the residue Y220 is completely conserved in the four
156 complexes, while S172 and T149 in hT1R1-T1R3 are replaced by threonine and serine in both
157 T1R2a-T1R3 and mGluR, respectively (Fig 3B and 3C). Moreover, the residue D147 in hT1R1-
158 T1R3 is replaced by glutamine and glycine in fish T1R2a-T1R3 and mGluR, respectively (S1 Fig)
159 [23], which may lead to the fact that the taste stimuli are different for varied species. Taken
160 together, our MSG-bound hT1R1-T1R3 VFD complex provides a fairly good starting structure
161 for the following MD simulations.



162

163 **Fig 4.** Interaction networks between umami ligands with hT1R1-VFD in each docking complex, including
164 WSA **(A)**, GMP **(B)**, IMP **(C)**, and BMP **(D)**. In each complex, the ligand is shown in cyan sticks, and the key
165 residues that form direct contacts with the ligand are shown in green/blue/violet sticks. Several key HBs
166 are highlighted with black dashed lines.

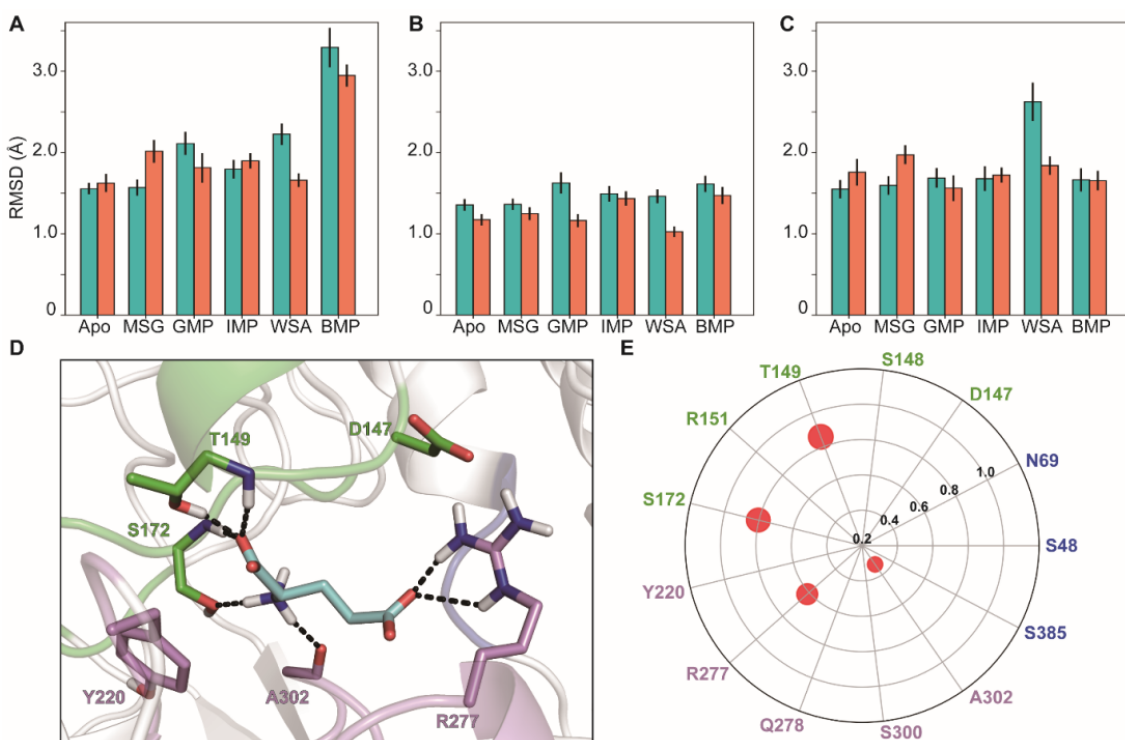
167 We then docked the other four ligands (WSA, GMP, IMP, and BMP) into the same binding
168 pocket as that for MSG. In the WSA binding complex, one of its COO⁻ group sits in the same
169 site as the C_α-COO⁻ group of MSG, while the other COO⁻ group can form HBs with the residues
170 A302 and S300 (Fig 4A). In addition, WSA can form hydrophobic contacts with Y220 (Fig 4A).
171 For the GMP and IMP binding complexes, the two ligands bind to hT1R1-T1R3 VFD in a very
172 similar mode (Fig 4B and 4C). The nucleobase of these ligands can form hydrophobic contacts
173 with Y220 and several HBs with S172 and T149, while the phosphate group can reach into
174 another pocket and form HBs with S276, S48, N69, and R277. Finally, in the BMP-bound
175 complex, the peptide BMP binds in the same pocket as that for the phosphate group of GMP
176 and IMP (Fig 4B, 4C, and 4D). In specific, the BMP can form HBs with the side-chain of R151
177 through its C-terminal A8. Moreover, the negatively charged residues D3, E4, E5 of BMP can
178 also form HBs with the residues A302, Y220, S276, R277, S385, and N69 (Fig 4D).

179 Taken the above results together, two major binding sites exist in the ligand-binding pocket
180 of hT1R1-VFD, one is surrounded by the LB1 residues D147, T149, R151, A170, and S172 (Figs
181 3A and 4, shown in green sticks), termed as site A; another consists of the LB1 residues S48,
182 N69, H71, S384, and S385 (Fig 4, shown in blue sticks), termed as site B. In particular, the LB2
183 residues Y220, S276, R277, Q278, S300, A302, and W303 (Figs 3A and 4, shown in violet sticks)
184 are shared by these two binding sites.

185

186 **Effects of ligand binding on structural dynamics of hT1R1-T1R3 VFD**

187 To study the effects of the ligand binding on the structural dynamics of hT1R1-T1R3 VFD, we
188 performed MD simulations starting from the above five ligand-bound hT1R1-T1R3 VFD
189 complexes. For each system, we performed two parallel 100-ns MD simulations initiated from
190 different velocities. As a control, we performed additional 100-ns MD simulations for the apo
191 hT1R1-T1R3 VFD (without ligand). To examine whether the system reaches equilibration
192 within 100-ns MD simulation, we firstly calculated the root-mean-square deviations (RMSD)
193 along the simulation time for each system using the minimized apo hT1R1-T1R3 VFD structure
194 as the reference structure. The results show that the RMSD curves tend to level off after ~80-
195 ns for each system (S3 Fig). We thus only kept the last 20-ns simulation data of each system
196 for further analysis.



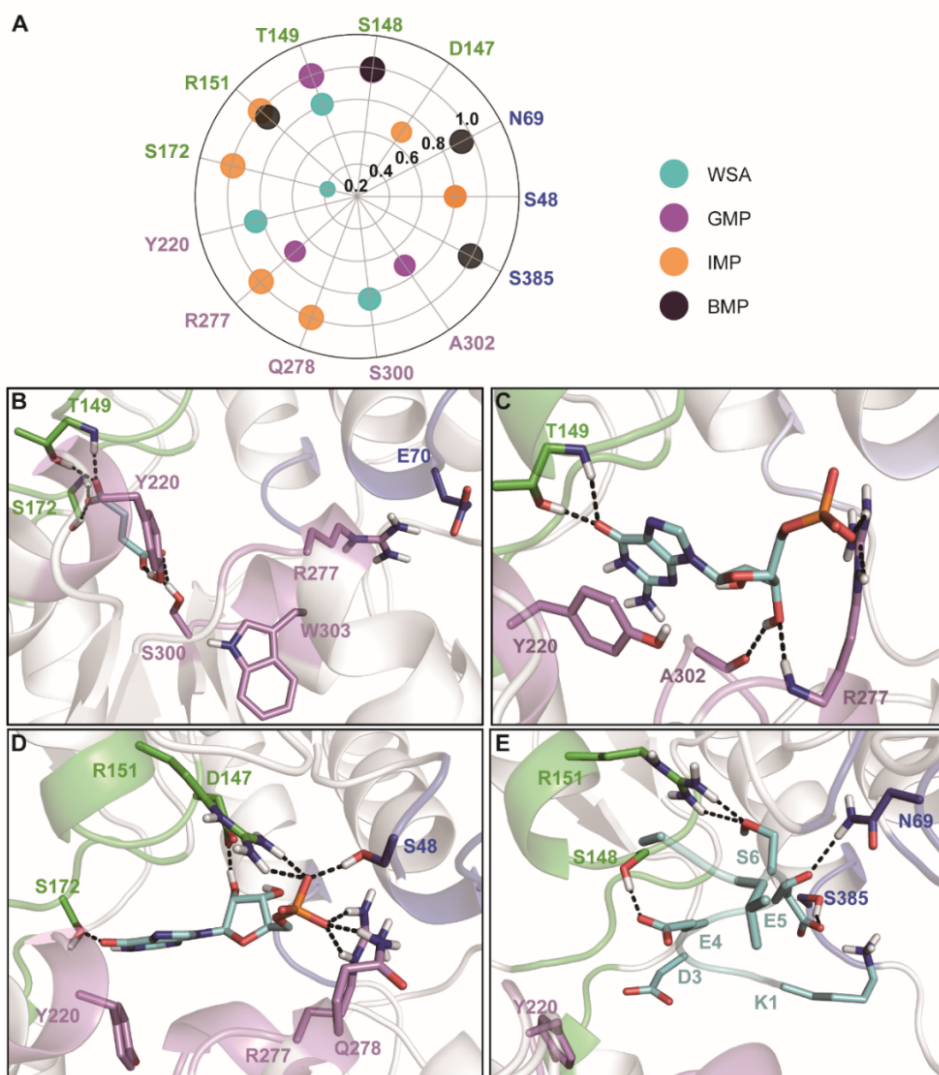
197

198 **Fig 5.** Effects of the ligand bindings on the receptor dynamics and HB network analysis for the MSG-bound
 199 hT1R1-VFD complex. RMSD of LB1+LB2 (**A**), LB1 (**B**), and LB2 (**C**) regions calculated based on two-parallel
 200 100-ns MD simulations (shown in cyan and coral, respectively). For each system, the mean RMSD and the
 201 corresponding standard error were calculated for the last 20-ns simulation conformations. (**D**) The binding
 202 mode of MSG (shown in cyan sticks) with hT1R1-VFD, the structure is derived from the last snapshot of the
 203 100-ns MD simulation. The key residues that form direct contacts with MSG are shown in green/blue/violet
 204 sticks. Several key HBs are highlighted with black dashed lines. (**E**) The HB network map for the MSG-bound
 205 hT1R1-VFD complex. The residues that can form HB with MSG are highlighted with red dot, with the dot
 206 size corresponding to the HB occupancy.

207 For each system, we further calculated the RMSD values for the C_{α} atoms of three different
 208 parts of hT1R1-VFD, namely LB1+LB2, LB1, and LB2, by firstly fitting to the corresponding
 209 regions to the apo hT1R1-VFD structure. The results show that comparing to LB1, the LB2 and
 210 LB1+LB2 domains demonstrates relatively higher structural fluctuations, reflected from their
 211 larger RMSD values, which suggests that LB1 keeps relatively rigid compared to LB2 during
 212 the simulations (Fig 5A, 5B, and 5C). Therefore, to better characterize the recognition

213 mechanism of these ligands, the LB1 domain of the apo hT1R1-VFD is used as a reference for
214 the further analysis. Moreover, the RMSD calculations indicate that the apo system
215 demonstrates relatively small structural fluctuations compared to the ligand-bound
216 complexes (Fig 5A, 5B, and 5C), suggesting the ligand binding can impose some structural
217 change of hT1R1-VFD. On the other hand, among the ligand-bound systems, the BMP-bound
218 complex exhibits the largest RMSD values for the LB1+LB2 regions, likely due to the relatively
219 bigger molecular size of BMP (Fig 5A). The other ligand-bound systems, however, have similar
220 structural fluctuations for the LB1+LB2 regions (Fig 5A). Notably, the paralleled MD
221 simulations for each system can reproduce the structural features of hT1R1-VFD structure
222 fairly well (Fig 5A, 5B, and 5C), we thus only used one of the two MD simulations for the
223 further analysis.

224 We next analyzed the interacting networks between each ligand and hT1R1-VFD by
225 calculating the hydrogen bond occupation (OC_{HB}). We only consider the HB that sustains
226 longer than 30 % of the simulation time for further structural analysis. In the MSG system,
227 four residues, namely T149, S172, R277, and A302, can form stable HBs with MSG, among
228 which T149 exhibits the highest OC_{HB} (85.8 %) and A302 exhibits the lowest OC_{HB} (32.9 %) (Fig
229 5E). In specific, T149 and S172 forms HBs with the C_{α} -COO⁻ group of MSG in the binding site
230 A, as observed in the initial docking complex (Fig 3A). Moreover, R277 can form HB with the
231 side-chain COO⁻ group of MSG, and notably, it can also form a salt bridge with D147, which
232 may strengthen the MSG binding (Fig 5D).



233

234 **Fig 6. (A)** The HB network map for four ligand-bound hT1R1-VFD complexes, including WSA, GMP, IMP,
 235 and BMP. **(B-E)** The binding mode of each ligand (shown in cyan sticks) with hT1R1-VFD, namely WSA **(B)**,
 236 GMP **(C)**, IMP **(D)**, and BMP **(E)**. The structures are derived from the last snapshot of the 100-ns MD
 237 simulation for each system. The ligand is shown in cyan sticks, and the residues that form direct contacts
 238 with the ligand are shown in green/blue/violet sticks. Several key HBs are highlighted with black dashed
 239 lines.

240 Similar HB analyses were performed for other ligand-bound systems. In the WSA-bound
 241 complex, four residues, Y220, S300, T149, and S172, can form stable HBs with the COO⁻ groups
 242 of WSA, among which Y220 exhibits the highest OC_{HB} (84.5 %) and S172 exhibits the lowest
 243 OC_{HB} (38.8 %) (Fig 6A and 6B). In specific, T149 and S172 in the binding site A can form HBs

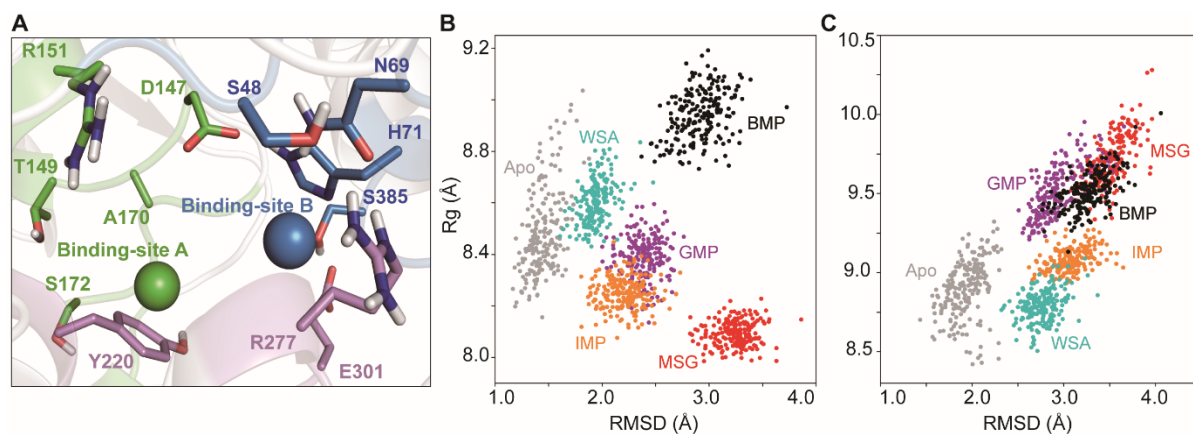
244 with one of the COO⁻ groups, and the other COO⁻ group can form stable HBs with Y220 and
245 S300 (Fig 6B). It is noteworthy that WSA is unable to bind to the binding site B. In the GMP-
246 bound complex, the ligand can form HBs with T149, A302, and R277, among which T149
247 exhibits the highest OC_{HB} (99.6 %) and R277 exhibits the lowest OC_{HB} (71.2 %) (Fig 6A and 6C).
248 In the IMP-bound complex, however, six residues, Q278, R151, R277, S172, S48, and D147,
249 form stable HBs with the substrate, and D147 exhibits relatively low OC_{HB} (68.3 %) compared
250 to other five residues (all > 80 %) (Fig 6A and 6D). Notably, GMP and IMP both sit in the same
251 pocket, with their phosphate group forming HB with R277 in the binding site B. Whereas
252 several HBs can be formed between IMP and R151, which is absent in GMP complex (Fig 6C
253 and 6D). Finally, in the BMP-bound complex, BMP largely sits in the binding site B, and forms
254 HBs with S148, S385, R151, and N69, with the OC_{HB} value all higher than 80 % (Fig 6E). The
255 above HBs are formed through the BMP residues E4, E5, and S6. In specific, the side-chain
256 COO⁻ of E4 forms HB with the side-chain of S148, and BMP E5 forms HBs with N69 and S385
257 (Fig 6E). In addition, BMP S6 can form HB with the side-chain of R151, and an intermolecular
258 HB can also be formed in BMP between K1 and E5.

259 Our HB analysis is consistent with our previous conclusion that, in general, the ligands
260 largely interact with two binding sites in hT1R1-VFD, and in each site, several polar residues
261 within the binding pocket that can potentially form HBs with the incoming ligand, as shown
262 in Figs 5E and 6A. Based on varied molecular size and chemical groups of the incoming ligand,
263 one or both of the above two sites can be occupied, i.e., MSG and WSA largely sit in the site
264 A, while BMP binds to the site B; GMP and IMP, on the other hand, can occupy both binding
265 sites. Therefore, we can expect that varied ligands may impose structural changes of hT1R1-
266 VFD in different manners, which in turn can induce distinct umami intensities.

267

268 Effects of ligand bindings on the opening/closing motions of hT1R1-VFD

269 Previous studies have suggested that the opening/closing motions of VFD are critical for
270 ligand binding [20]. To measure the effects of the ligands on the opening/closing motions of
271 hT1R1-VFD, we calculated the radius of gyration (Rg) values for the two identified ligand
272 binding sites (A and B) in hT1R1-VFD, which can roughly measure the extents of the hT1R1-
273 VFD opening/closing. Both sites contain the LB2 residues 219-221, 276-278, 300-303, and in
274 site A, we also include the LB1 residues 146-151, 170-173 (shown in green and violet in Fig
275 7A), and in binding site B, the LB1 residues 47-49, 68-71, 384-386 are included (shown in blue
276 and violet in Fig 7A). For each binding site, we then projected the MD conformations onto
277 two reaction coordinates: Rg and RMSD, calculated for the binding site residues (Fig 7B and
278 7C).



279
280 **Fig 7.** The opening/closing motions of hT1R1-VFD induced by ligand binding. **(A)** To investigate the closing
281 and opening motions of hT1R1-VFD, two binding sites (A and B) are defined and represented with green
282 and blue sphere, respectively. Each sphere represents the centroid of C α atoms of residues within each
283 binding site. In specific, both binding sites include the LB2 residues 219-221, 276-278, 300-303 (shown in
284 violet). In addition, the site A also contains the LB1 residues 146-151, 170-173 (shown in green), and the
285 site B contains the LB1 residues 47-49, 68-71, 384-386 (shown in blue). For the binding site A **(B)** and B **(C)**,
286 we mapped the MD conformations onto two reaction coordinates: one is the Rg of the residues belonging
287 to each site, another one is the corresponding RMSD.

288 For binding site A, by treating the apo system as a ground state, we can group the five
289 ligands into two classes (Fig 7B). One group includes WSA and BMP that prefer to increase
290 the Rg value of the binding site A, suggesting that they can potentially promote the opening
291 of hT1R1-VFD. In contrast, the other group, consisting of MSG, GMP, and IMP, can tighten the
292 site A, reflected from the reduced Rg values comparing to the apo system. However, it is
293 worth to note that within each group, the ligands also act differently on the protein dynamics,
294 reflected from both the Rg and RMSD calculations. In specific, BMP exerts much higher
295 structural disturbances on hT1R1-VFD than WSA, with an increased Rg and RMSD values, and
296 has stronger effects on promoting the opening of the binding site A compared to WSA. For
297 the second group, MSG tightens the binding site A the most compared to GMP and IMP,
298 reflected from its lowest Rg values (Fig 7B). GMP and IMP, on the other hand, can affect the
299 protein structure in a similar manner.

300 On the other hand, for binding site B, only WSA can slightly tighten the binding site B,
301 reflected from the reduced Rg value comparing to the apo system (Fig 7C), which is likely due
302 to the fact that WSA is unable to reach the binding site B. The other ligands, however, can all
303 promote the opening of binding site B, reflected from the increased Rg values comparing to
304 the apo system (Fig 7C). In specific, MSG, BMP, and GMP exert relatively larger effects on
305 promoting the hT1R1-VFD opening compared to IMP. It is noteworthy that although MSG
306 largely binds to site A, it tightens binding site A, whereas opens up binding site B (Fig 7B and
307 7C), we speculate that this is because MSG attracts more interactions from the LB2 residues,
308 e.g., Y220, R277, and A302, which induces the movements of LB2 towards site A.

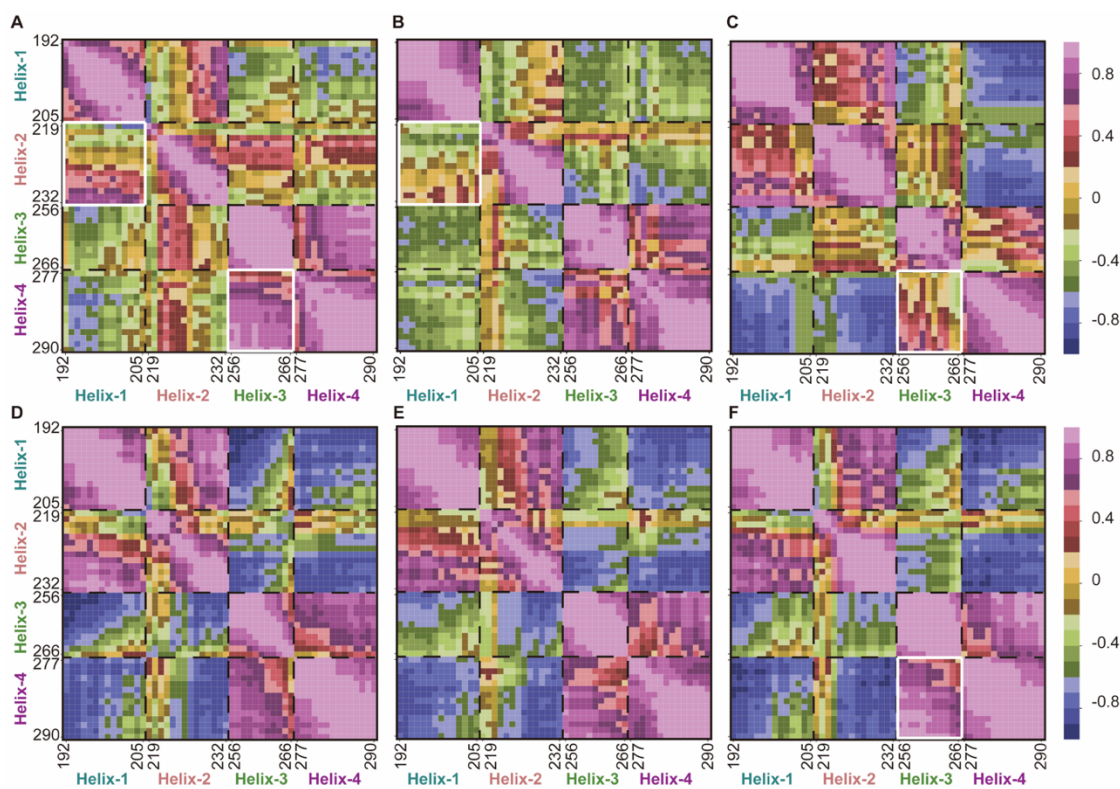
309 In conclusion, depending on the various incoming ligands, the hT1R1-VFD can undergo
310 either opening or closing motions. In particular, MSG, GMP, and IMP tend to promote the
311 closing of binding site A, while opening of binding site B. BMP, however, can promote the

312 opening of both two binding sites. Notably, WSA can also promote the opening of binding site
313 A, whereas slightly induce the closing of site B.

314

315 **Effects of ligand bindings on hT1R1 LB2 dynamics**

316 The hT1R1-VFD opening/closing induced by ligand binding may result in a structural
317 rearrangement of either LB1 or LB2 domain. Our previous analyses indicate that LB1 keeps
318 relatively rigid compared to LB2, therefore, we further examine the effects of ligand binding
319 on the dynamics of LB2. We thus pinpointed two helices (termed as 1 and 2) near to the
320 binding site A, and two other helices (termed as 3 and 4) near to the binding site B for the
321 following dynamic cross-correlation map (DCCM) analysis (Fig 2A). DCCM describes the
322 correlated motion for a residue pair, with a positive value representing positive correlation
323 (moving towards the same direction), while a negative value indicating the residue pair
324 moving towards the opposite direction (Fig 8).



325

326 **Fig 8.** Effects of ligand bindings on hT1R1-VFD dynamics. Cross-correlation matrices of four LB2 helices for
327 apo hT1R1 **(A)**, and five ligand-bound hT1R1-VFD complexes, namely MSG **(B)**, WSA **(C)**, GMP **(D)**, IMP **(E)**,
328 and BMP **(F)**. The correlation values were calculation based on the last 20-ns MD simulation dataset for
329 each system, with the value equal to 1 representing a positive correlation between two motions, and the
330 value equal to -1 representing a negative correlation between two motions.

331 The DCCM shows that the five ligands indeed exert different effects on the dynamics of the
332 LB2 domain. For the apo system, helix-1 and 2 have a weak correlation, and helix-3 and 4 have
333 a strong positive correlation (Fig 8A). In comparison, the MSG binding can further weaken the
334 correlation between helix-1 and 2, while has no obvious effect on the helix 3 and 4 (Fig 8B),
335 suggesting that MSG can interfere the interacting networks between helix 1 and 2. In addition,
336 GMP and IMP demonstrate very similar correlation values, suggesting that these two ligands
337 impose similar stresses on the binding sites in hT1R1-VFD, which is consistent with previous
338 results (Fig 8D and 8E). For WSA and BMP, their bindings give rise to a stronger positive
339 correlation between helix 1 and 2 compared to the apo system (Fig 8C and 8F), consistent
340 with the above analysis that they can both open up binding site A (Fig 7B). Moreover, WSA
341 tends to decorrelate helix 3 and 4 compared to all other systems, suggesting its potential role
342 in interrupting the interaction network between helix 3 and 4.

343 Taken the above results together, the ligand binding within the interface between LB1 and
344 LB2 can indeed affect the structure dynamics of LB2, likely through either tightening or
345 opening up the binding sites. In particular, the closing of binding site tends to weaken the
346 couplings between the adjacent helices, such as the effects of MSG on helix 1 & 2 and WSA
347 on helix 3 & 4.

348 **Discussion**

349 One of our major findings is to identify the key residues that directly recognize the five umami
350 ligands, which warrants further experimental studies to validate our theoretical models.
351 Former modeling and mutagenesis work has already identified several critical hT1R1-VFD
352 residues for MSG, such as S172, D192, Y220, E301, A170, and A302; moreover, H71, R277,
353 S306, and H308 were identified to be critical for GMP and IMP binding [3, 8]. This result is
354 well consistent with our theoretical models in which S172, A302 can form direct contacts with
355 MSG, and R277 is essential roles in recognizing GMP and IMP. In addition, Y220 can form
356 hydrophobic contacts with all the above three ligands (Figs 5D, 6C, and 6D). Therefore, the
357 constructed model of hT1R1-T1R3 VFD using the fish T1R2a-T1R3 as a template is reliable to
358 derive the binding complexes for umami ligands. Moreover, we can predict more mutational
359 effects on the substrate binding, such as WSA can form important contacts with S172, T149,
360 Y220, and S300 (Fig 6B); the residues T149 and A302 are found to be critical for GMP binding
361 (Fig 6C); five residues R151, S148, N69, Y220, and S385 can directly interact with BMP (Fig 6E).
362 Notably, we can see that the afore-mentioned residues are not highly conserved among
363 different species, such as, S48, N69, D147, R151, A170, Q278, and S385 in hT1R1-VFD are
364 completely non-conservative in fish, rat, and mouse (S1 Fig). Interestingly, former
365 luminescence intensities assay have shown that L-Glu can induce higher umami intensities to
366 hT1R1-T1R3 than mT1R1-T1R3, indicating the sequence differences in the two receptors
367 indeed influences the umami responses [8]. Therefore, our model suggests that these non-
368 conservative residues may contribute to the distinct umami intensities for different species.

369 More importantly, we find that hT1R1-VFD contains two major binding sites for the umami
370 ligands, and the molecular size and carried charges of the incoming ligand determine its
371 favored binding sites. In specific, MSG and WSA can largely sit in the binding site A, BMP binds

372 to the binding site B, while GMP and IMP can occupy both sites (Figs 5 and 6). From a
373 structural perspective, the site B has a larger binding pocket than site A, which allows the
374 binding of relatively bigger chemical groups (Figs 3A and 7A). On the other hand, to further
375 understand the charge preference for different binding sites, we calculated the electrostatics
376 potentials for hT1R1-VFD using Adaptive Poisson-Boltzmann Solver (APBS). The results
377 indicate that the binding site B is more positively charged compared to binding site A (S4 Fig).
378 In summary, we thus speculate that ligand with large molecular size and negatively charges
379 tends to bind to binding site B, for example, E4 and E5 in BMP, and the phosphate group of
380 GMP and IMP (Fig 6C, 6D, and 6E).

381 Former experimental studies have shown that the umami threshold value of BMP (1.41
382 mM) is lower than MSG (1.56 mM), indicating that the taste receptor is more sensitive to BMP
383 than MSG [24]. Moreover, Zhang et al., using the fluorescence imaging plate reader (FLIPR),
384 studied the molecular mechanism of umami synergism for GMP and IMP [3]. They found that
385 both ligands can enhance the umami stimuli of L-Glu. These studies indicate that different
386 umami substances might impose different effects on the protein dynamics. As shown above,
387 different umami ligands can occupy one or both of the two binding sites, leading to distinct
388 closing/opening motions of hT1R1-VFD. For example, BMP promotes the binding site A
389 opening, while MSG tends to close the binding site A. Considering these two ligands have
390 different umami threshold values, we thus speculate the umami properties of the two ligands
391 may relate to their different effects exerted on the protein dynamics. On the other hand, GMP
392 and IMP can impose similar structural influences on the receptor, i.e., they can both induce
393 the closing of binding site A, which lead to a similar dynamic properties of the hT1R1 LB2
394 region (Fig 8D and 8E). This finding may explain the experimental observation that GMP and

395 IMP have similar umami intensities. Taken together, our work provides a structural basis for
396 relating the effects of ligand binding to the resulting umami signals.

397

398 **Conclusions**

399 In this work, by employing homology modeling, molecular docking, and MD simulations, we
400 constructed the ligand-bound hT1R1-T1R3 VFD complexes for five natural umami ligands and
401 revealed how the ligand bindings affect the dynamics of hT1R1-VFD. We identified the key
402 residues that play essential roles in recognizing the ligands, some of the results are supported
403 by former site-directed mutagenesis studies [3, 8]. Further interacting network analysis
404 indicates that two major adjacent binding sites exist in the cleft region of hT1R1-VFD. More
405 interestingly, we find that depending on the molecular size and chemical properties, the
406 incoming ligand can sit in one or both of these two binding sites, which in turn can regulate
407 the closing and opening motions of hT1R1-VFD. In conclusion, our work reveal, at an
408 atomistic-level, the structural basis for the functional roles of different umami ligands in
409 regulating the dynamics of hT1R1-T1R3, and provides further guidance for designing more
410 effective umami ligands.

411

412 **Methods**

413 **Constructing the hT1R1-T1R3 VFD structure using homology modeling**

414 By employing the structure of fish taste receptor T1R2a-T1R3 (PDB id: 5X2M) as a homology
415 template, we constructed the model of hT1R1-T1R3 VFD using SWISS-MODEL software [25].
416 The target amino acid sequences of hT1R1-T1R3 VFD was acquired from the universal protein
417 resource knowledgebase (UniProKB) (HT1R1, Q7RTX1; HT1R3, Q7RTX0). The fish T1R2a-T1R3

418 was used for the homology modeling because it exhibits the highest sequence identity with
419 hT1R1-T1R3 VFD compared to other homologues (S1 Fig). Moreover, a phylogenetic tree was
420 constructed to further prove that the fish T1R2a-T1R3 is the best template so far for the
421 model construction. In specific, the T1R and mGluR were selected to construct the
422 phylogenetic tree based on their VFD, sourced from human T1R1 (h-T1R1, UniProtKB:
423 Q7RTX1), human T1R2 (h-T1R2, UniProtKB: Q8TE23), human T1R3 (h-T1R3, UniProtKB:
424 Q7RTX0), mouse T1R1 (m-T1R1, UniProtKB: Q99PG6), mouse T1R2 (m-T1R2, UniProtKB:
425 Q925I4), mouse T1R3 (m-T1R3, UniProtKB: Q925D8), rat T1R1 (r-T1R1, UniProtKB: Q9Z0R8),
426 rat T1R2 (r-T1R2, UniProtKB: Q9Z0R7), rat T1R3 (r-T1R3, UniProtKB: Q923K1), fish T1R2a (f-
427 T1R2a, PDBID: 5X2M), fish T1R3 (f-T1R3, PDBID: 5X2M), human mGluR1 (h-mGluR1,
428 UniProtKB: Q13255), human mGluR4 (h-mGluR4, UniProtKB: Q14833), mouse mGluR1 (m-
429 mGluR1, UniProtKB: P97772), mouse mGluR4 (m-GluR4, UniProtKB: Q68EF4), rat mGluR1 (r-
430 mGluR1, UniProtKB: P23385), and rat mGluR4 (r-mGluR4, UniProtKB: P31423).

431

432 **Obtaining initial ligand-bound hT1R1-T1R3 VFD complex using molecular docking**

433 By using Gauss View 5 and AMBER 14 software [26, 27], the structure of five umami ligands
434 were constructed, including MSG, WSA, GMP, IMP, and BMP. Then, we performed molecular
435 docking for the above five ligands to hT1R1-VFD using the AutoDock vina-1.1.2 software
436 package with the default scoring function [28]. The docking cube grid box size is set to 30 Å,
437 and the center of grid box is set as the center of mass of L-Gln in the homology template
438 structure. The PDBQT of receptor and ligands was calculated by AutoDock Tools-1.5.6
439 package [29, 30].

440

441 **Setup of MD simulations**

442 Each ligand-bound hT1R1-T1R3 VFD complex was centered in a cubic box with the size of 10
443 Å, and filled with TIP3P water. A appropriate number of Na⁺ and Cl⁻ were added in the water
444 box by randomly replacing the solvent waters to neutralize the system and ensure an ionic
445 concentration of 0.15 M. The cutoff distances for Van der Waals and short-range electrostatic
446 interactions were set to 12 Å, and the long-range electrostatic interactions were treated using
447 the Particle-Mesh Ewald (PME) [31]. The SHAKE algorithm was used to constrain all the
448 chemical bonds [32]. The AMBER14SB force field was employed to describe the hT1R1-T1R3
449 VFD structure, and the AMBER force fields of ligands were generated using the antechamber
450 module implemented in the Amber-Tools package, and the RESP charges were calculated
451 using the Hartree-Fork methods under the basis set 6-31+g (d) [15, 33, 34].

452 Energy minimization was firstly performed for each complex by combing the steepest
453 descent and conjugate gradient methods, consisting of the following three steps: (1) with all
454 the heavy atoms of the system constrained with a force constant of 10 kcal/mol/Å⁻²; (2) With
455 all the C_α atoms of the system constrained with a force constant of 10 kcal/mol/ Å⁻²; (3) All
456 the atoms are fully relaxed. After minimization, the system temperature was gradually
457 increased from 0 k to 300 k within 100 ps. Then, we performed two 100-ps constrained MD
458 simulations for each complex, with all the heavy atoms constrained with 10 kcal/mol/ Å⁻² and
459 5 kcal/mol/ Å⁻², respectively. Finally, two parallel non-constrained 100-ns NPT MD simulations
460 were conducted under NVT ensemble, each initiated with different velocities. The
461 temperature was kept at 300K using the Langevin Thermostat [35].

462

463 **HB and DCCM analysis**

464 One HB was defined as that the distance between that acceptor heavy atom A and a donor
465 heavy atom D is less than 3.5 Å, and the angle formed by atom A, donor H atom and atom D
466 is greater than 135°. The OC_{HB} were determined by the following equation:

$$467 \quad OC_{HB} = \frac{n}{N} \times 100\%$$

468 Where n indicates a number of frames that formed HB during MD simulation, N indicates the
469 total number of frames. The PYMOL 2.0 (The PyMOL Molecular Graphics System, Version 2.0
470 Schrödinger, LLC.) and Visual Molecular Dynamics (VMD 1.9.4a12) [36] were used to analyze
471 and visualize the ligand-bound complex.

472 DCCM was performed to investigate the correlated motions between four helices from
473 hT1R1 LB2 region. Before constructing the covariance matrix (C_{ij}), all the MD configurations
474 were fitted to the reference structure, then C_{ij} is determined by the following equation:

$$475 \quad C_{ij} = \frac{\langle \Delta r_i \cdot \Delta r_j \rangle}{\sqrt{\langle \Delta r_i \cdot \Delta r_i \rangle \langle \Delta r_j \cdot \Delta r_j \rangle}}$$

476 Where the angle bracket represents the average of coordinate over the MD simulation
477 trajectory, and Δr_i indicates the deviation of the C_α atom of the i th residue from its mean
478 position [37, 38]. The value of C_{ij} fluctuates from -1 to 1. When the value of C_{ij} is positive, it
479 represents a positive correlated motion between the i th residue and the j th residue,
480 otherwise, it is negatively correlated motion.

481

482 **Supporting information captions**

483 **S1 Fig. Sequence alignment of the N-Venus Flytrap domain (VFD) in T1R and mGluR1.** The
484 amino acid sequences of VFD from human T1R1 (HT1R1, UniProtKB: Q7RTX1), human T1R3
485 (HT1R3, UniProtKB: Q7RTX0), rat T1R1 (RT1R1, UniProtKB: Q9ZOR8), rat T1R3 (RT1R3,
486 UniProtKB: Q923K1), fish T1R2a-T1R3 (FT1R2a-T1R3, PDBID: 5X2M), and mGluR1 (PDBID:

487 1EWK) were aligned by blast module of NCBI, and adjusted by ESPript 3.0. The residues 219-
488 221, 276-278, 300-303 are highlighted in violet border; the residues 146-151, 170-173 are
489 highlighted in green border, and the residues 47-49, 68-71, 384-386 are highlighted in blue
490 border. Moreover, the residues that form direct contacts with the five ligand are highlighted
491 with red star. In addition, for FT1R3, the residues that are critical for L-glutamine's binding
492 are highlighted with coral rectangle. In mGluR1, the residues that play essential roles in
493 recognizing the L-glutamate are highlighted with blue ellipse.

494 **S2 Fig. Phylogenetic tree for T1R and mGluR from different species.** The phylogenetic tree
495 was constructed using the amino acid sequences of T1R and mGluR VFD, sourced from human
496 T1R1 (h-T1R1, UniProtKB: Q7RTX1), human T1R2 (h-T1R2, UniProtKB: Q8TE23), human T1R3
497 (h-T1R3, UniProtKB: Q7RTX0), mouse T1R1 (m-T1R1, UniProtKB: Q99PG6), mouse T1R2 (m-
498 T1R2, UniProtKB: Q925I4), mouse T1R3 (m-T1R3, UniProtKB: Q925D8), rat T1R1 (r-T1R1,
499 UniProtKB: Q9Z0R8), rat T1R2 (r-T1R2, UniProtKB: Q9Z0R7), rat T1R3 (r-T1R3, UniProtKB:
500 Q923K1), fish T1R2a (f-T1R2a, PDBID: 5X2M), fish T1R3 (f-T1R3, PDBID: 5X2M), human
501 mGluR1 (h-mGluR1, UniProtKB: Q13255), human mGluR4 (h-mGluR4, UniProtKB: Q14833),
502 mouse mGluR1 (m-mGluR1, UniProtKB: P97772), mouse mGluR4 (m-GluR4, UniProtKB:
503 Q68EF4), rat mGluR1 (r-mGluR1, UniProtKB: P23385), and rat mGluR4 (r-mGluR4, UniProtKB:
504 P31423).

505 **S3 Fig. Effects of the ligand bindings on the receptor dynamics.** Root mean square deviations
506 (RMSD) of LB1+LB2, LB1, and LB2 regions calculated based on two-parallel 100-ns MD
507 simulations (named run-1 and run-2, respectively). For each system, the RMSD along the
508 simulation time was calculated for the 100-ns simulation dataset.

509 **S4 Fig. The electrostatics potential of hT1R1-VFD.** Positive and negative potential is shown in
510 blue and red, respectively.

511

512 **Author Contributions**

513 **Conceptualization:** Hai Liu, Lin-Tai Da, Yuan Liu.

514 **Data curation:** Hai Liu.

515 **Formal analysis:** Hai Liu, Lin-Tai Da.

516 **Funding acquisition:** Yuan Liu.

517 **Methodology:** Hai Liu, Lin-Tai Da, Yuan Liu.

518 **Project administration:** Yuan Liu.

519 **Supervision:** Yuan Liu, Lin-Tai Da.

520 **Writing - original draft:** Hai Liu.

521 **Writing – review & editing:** Hai Liu, Lin-Tai Da, Yuan Liu.

522

523 **References**

524 1. Ikeda K. New seasonings. *Chem Senses*. 2002; 27(9):847-849.

525 <https://doi.org/10.1093/chemse/27.9.847> PMID: [12438213](https://pubmed.ncbi.nlm.nih.gov/12438213/)

526 2. Nelson G, Chandrashekar J, Hoon MA, Feng LX, Zhao G, Ryba NJP, et al. An amino-acid

527 taste receptor. *Nature*. 2002; 416(6877):199-202. <https://doi.org/10.1038/nature726>

528 PMID: [11894099](https://pubmed.ncbi.nlm.nih.gov/11894099/)

529 3. Zhang F, Klebansky B, Fine RM, Xu H, Pronin A, Liu HT, et al. Molecular mechanism for

530 the umami taste synergism. *P Natl Acad Sci USA*. 2008; 105(52):20930-20934.

531 <https://doi.org/10.1073/pnas.0810174106> PMID: [19104071](https://pubmed.ncbi.nlm.nih.gov/19104071/)

- 532 4. Li X, Staszewski L, Xu H, Durick K, Zoller M, Adler E. Human receptors for sweet and
533 umami taste. Proc Natl Acad Sci U S A. 2002; 99(7):4692-4696.
534 <https://doi.org/10.1073/pnas.072090199> PMID: [11917125](https://pubmed.ncbi.nlm.nih.gov/11917125/)
- 535 5. Pin JP, Kniazeff J, Goudet C, Bessis AS, Liu J, Galvez T, et al. The activation mechanism of
536 class-C G-protein coupled receptors. Biol Cell. 2004; 96(5):335-342.
537 <https://doi.org/10.1016/j.biolcel.2004.03.005> PMID: [15207901](https://pubmed.ncbi.nlm.nih.gov/15207901/)
- 538 6. Li XD. T1R receptors mediate mammalian sweet and umami taste. Am J Clin Nutr. 2009;
539 90(3):733s-737s. <https://doi.org/10.3945/ajcn.2009.27462G> PMID: [19656838](https://pubmed.ncbi.nlm.nih.gov/19656838/)
- 540 7. Zhang F, Klebansky B, Fine RM, Liu HT, Xu H, Servant G, et al. Molecular mechanism of
541 the sweet taste enhancers. P Natl Acad Sci USA. 2010; 107(10):4752-4757.
542 <https://doi.org/10.1073/pnas.0911660107> PMID: [20173095](https://pubmed.ncbi.nlm.nih.gov/20173095/)
- 543 8. Toda Y, Nakagita T, Hayakawa T, Okada S, Narukawa M, Imai H, et al. Two Distinct
544 Determinants of Ligand Specificity in T1R1/T1R3 (the Umami Taste Receptor). J Biol
545 Chem. 2013; 288(52):36863-36877. <https://doi.org/10.1074/jbc.M113.494443> PMID:
546 [24214976](https://pubmed.ncbi.nlm.nih.gov/24214976/)
- 547 9. Narukawa M, Toda Y, Nakagita T, Hayashi Y, Misaka T. L-Theanine elicits umami taste
548 via the T1R1+T1R3 umami taste receptor. Amino Acids. 2014; 46(6):1583-1587.
549 <https://doi.org/10.1007/s00726-014-1713-3> PMID: [24633359](https://pubmed.ncbi.nlm.nih.gov/24633359/)
- 550 10. Toda Y, Nakagita T, Hirokawa T, Yamashita Y, Nakajima A, Narukawa M, et al.
551 Positive/Negative Allosteric Modulation Switching in an Umami Taste Receptor
552 (T1R1/T1R3) by a Natural Flavor Compound, Methional. Sci Rep-Uk. 2018; 8(1):11796-
553 11808. <https://doi.org/10.1038/s41598-018-30315-x> PMID: [30087430](https://pubmed.ncbi.nlm.nih.gov/30087430/)
- 554 11. Trzaskowski B, Latek D, Yuan S, Ghoshdastider U, Debinski A, Filipek S. Action of
555 Molecular Switches in GPCRs - Theoretical and Experimental Studies. Curr Med Chem.

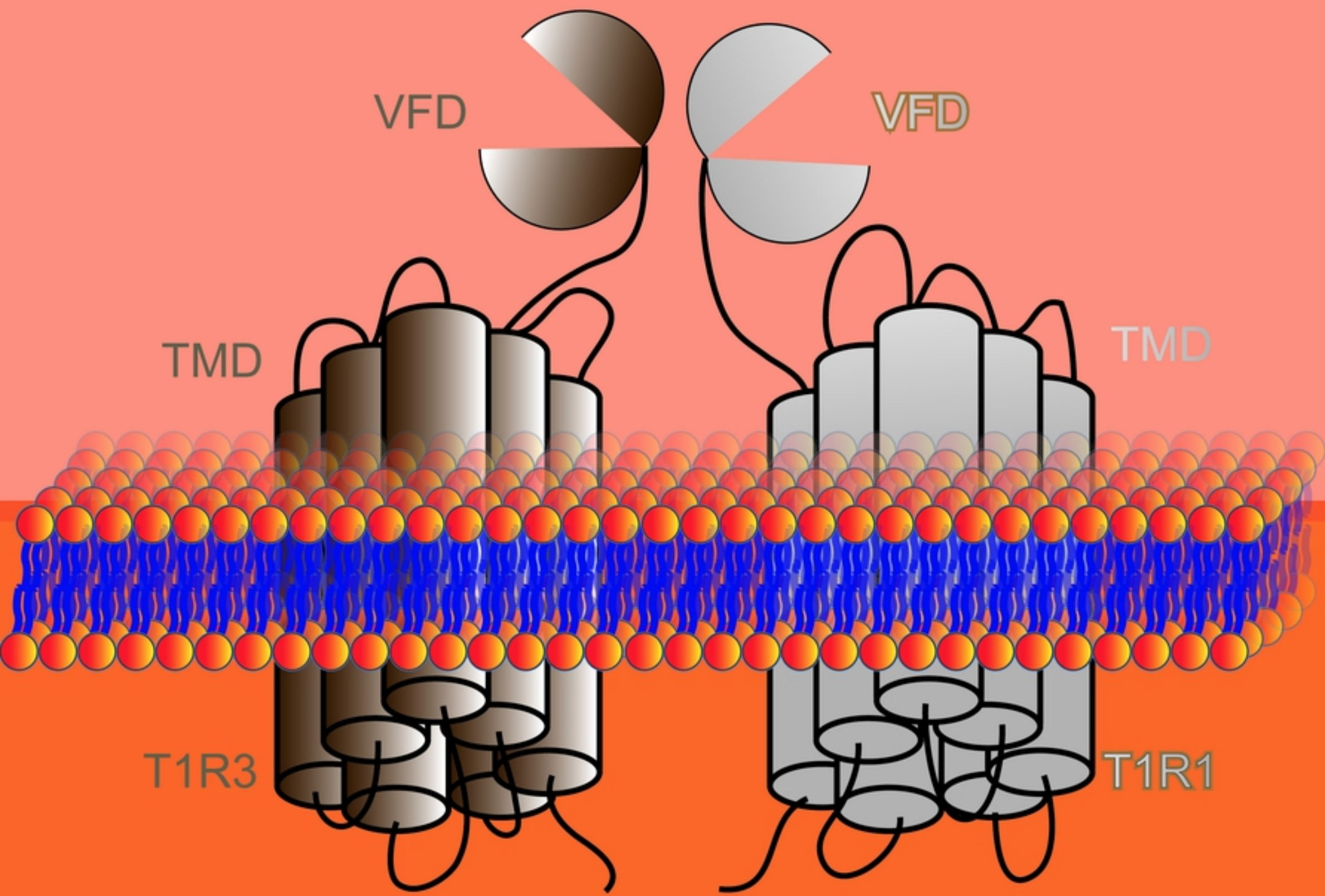
- 556 2012; 19(8):1090-1109. <https://doi.org/10.2174/092986712799320556> PMID:
557 [22300046](https://doi.org/10.2174/092986712799320556)
- 558 12. Yamaguchi S, Ninomiya K. Umami and food palatability. *J Nutr.* 2000; 130(4):921s-926s.
559 https://doi.org/10.1007/978-1-4615-4693-1_36 PMID: [10736353](https://pubmed.ncbi.nlm.nih.gov/10736353/)
- 560 13. Su GW, Cui C, Zheng L, Yan B, Ren JY, Zhao MM. Isolation and identification of two
561 novel umami and umami-enhancing peptides from peanut hydrolysate by consecutive
562 chromatography and MALDI-TOF/TOF MS. *Food Chem.* 2012; 135(2):479-485.
563 <https://doi.org/10.1016/j.foodchem.2012.04.130> PMID: [22868117](https://pubmed.ncbi.nlm.nih.gov/22868117/)
- 564 14. Dang YL, Gao XC, Ma FM, Wu XQ. Comparison of umami taste peptides in water-soluble
565 extractions of Jinhua and Parma hams. *Lwt-Food Sci Technol.* 2015; 60(2):1179-1186.
566 <https://doi.org/10.1016/j.lwt.2014.09.014>
- 567 15. Yu XQ, Zhang LJ, Miao XD, Li YY, Liu Y. The structure features of umami hexapeptides
568 for the T1R1/T1R3 receptor. *Food Chem.* 2017; 221:599-605.
569 <https://doi.org/10.1016/j.foodchem.2016.11.133> PMID: [27979247](https://pubmed.ncbi.nlm.nih.gov/27979247/)
- 570 16. Cascales JJL, Costa SDO, de Groot BL, Walters DE. Binding of glutamate to the umami
571 receptor. *Biophys Chem.* 2010; 152(1-3):139-144.
572 <https://doi.org/10.1016/j.bpc.2010.09.001> PMID: [20961679](https://pubmed.ncbi.nlm.nih.gov/20961679/)
- 573 17. Dang YL, Gao XC, Xie AY, Wu XQ, Ma FM. Interaction Between Umami Peptide and
574 Taste Receptor T1R1/T1R3. *Cell Biochem Biophys.* 2014; 70(3):1841-1848.
575 <https://doi.org/10.1007/s12013-014-0141-z> PMID: [25331670](https://pubmed.ncbi.nlm.nih.gov/25331670/)
- 576 18. Dang YL, Hao L, Cao JX, Sun YY, Zeng XQ, Wu Z, et al. Molecular docking and simulation
577 of the synergistic effect between umami peptides, monosodium glutamate and taste
578 receptor T1R1/T1R3. *Food Chem.* 2019; 271:697-706.
579 <https://doi.org/10.1016/j.foodchem.2018.08.001> PMID: [30236733](https://pubmed.ncbi.nlm.nih.gov/30236733/)

- 580 19. Nuemket N, Yasui N, Kusakabe Y, Nomura Y, Atsumi N, Akiyama S, et al. Structural basis
581 for perception of diverse chemical substances by T1r taste receptors. *Nat Commun.*
582 2017; 8:15530-15539. <https://doi.org/10.1038/ncomms15530> PMID: [28534491](https://pubmed.ncbi.nlm.nih.gov/28534491/)
- 583 20. Kunishima N, Shimada Y, Tsuji Y, Sato T, Yamamoto M, Kumasaka T, et al. Structural
584 basis of glutamate recognition by a dimeric metabotropic glutamate receptor. *Nature.*
585 2000; 407(6807):971-977. <https://doi.org/10.1038/35039564> PMID: [11069170](https://pubmed.ncbi.nlm.nih.gov/11069170/)
- 586 21. Geng Y, Bush M, Mosyak L, Wang F, Fan QR. Structural mechanism of ligand activation
587 in human GABA(B) receptor. *Nature.* 2013; 504(7479):254-261.
588 <https://doi.org/10.1038/nature12725> PMID: [24305054](https://pubmed.ncbi.nlm.nih.gov/24305054/)
- 589 22. Damak S, Rong MQ, Yasumatsu K, Kokrashvili Z, Varadarajan V, Zou SY, et al. Detection
590 of sweet and umami taste in the absence of taste receptor T1r3. *Science.* 2003;
591 301(5634):850-853. <https://doi.org/10.1126/science.1087155> PMID: [12869700](https://pubmed.ncbi.nlm.nih.gov/12869700/)
- 592 23. Robert X, Gouet P. Deciphering key features in protein structures with the new
593 ENDscript server. *Nucleic Acids Res.* 2014; 42(W1):W320-W324.
594 <https://doi.org/10.1093/nar/gku316> PMID: [24753421](https://pubmed.ncbi.nlm.nih.gov/24753421/)
- 595 24. Tamura M, Nakatsuka T, Tada M, Kawasaki Y, Kikuchi E, Okai H. The Relationship
596 between Taste and Primary Structure of "Delicious Peptide" (Lys-Gly-Asp-
597 Glu-Glu-Ser-Leu-Ala) from Beef Soup. *Agricultural and Biological Chemistry.* 1989;
598 53(2):319-325. <https://doi.org/10.1271/bbb1961.53.319>
- 599 25. Waterhouse A, Bertoni M, Bienert S, Studer G, Tauriello G, Gumienny R, et al. SWISS-
600 MODEL: homology modelling of protein structures and complexes. *Nucleic Acids Res.*
601 2018; 46(W1):W296-W303. <https://doi.org/10.1093/nar/gky427> PMID: [29788355](https://pubmed.ncbi.nlm.nih.gov/29788355/)

- 602 26. Case DA, Cheatham TE, Darden T, Gohlke H, Luo R, Merz KM, et al. The Amber
603 biomolecular simulation programs. *J Comput Chem.* 2005; 26(16):1668-1688.
604 <https://doi.org/10.1002/jcc.20290> PMID: [16200636](https://pubmed.ncbi.nlm.nih.gov/16200636/)
- 605 27. Salomon-Ferrer R, Case DA, Walker RC. An overview of the Amber biomolecular
606 simulation package. *Wires Comput Mol Sci.* 2013; 3(2):198-210.
607 <https://doi.org/10.1002/wcms.1121>
- 608 28. Trott O, Olson AJ. Software News and Update AutoDock Vina: Improving the Speed and
609 Accuracy of Docking with a New Scoring Function, Efficient Optimization, and
610 Multithreading. *J Comput Chem.* 2010; 31(2):455-461.
611 <https://doi.org/10.1002/jcc.21334> PMID: [19499576](https://pubmed.ncbi.nlm.nih.gov/19499576/)
- 612 29. Morris GM, Huey R, Lindstrom W, Sanner MF, Belew RK, Goodsell DS, et al. AutoDock4
613 and AutoDockTools4: Automated Docking with Selective Receptor Flexibility. *J Comput*
614 *Chem.* 2009; 30(16):2785-2791. <https://doi.org/10.1002/jcc.21256> PMID: [19399780](https://pubmed.ncbi.nlm.nih.gov/19399780/)
- 615 30. Sotriffer CA, Flader W, Winger RH, Rode BM, Liedl KR, Varga JM. Automated docking of
616 ligands to antibodies: Methods and applications. *Methods.* 2000; 20(3):280-291.
617 <https://doi.org/10.1006/meth.1999.0922> PMID: [10694451](https://pubmed.ncbi.nlm.nih.gov/10694451/)
- 618 31. Essmann,U., Perera,L., Berkowitz,M.L., Darden,T., Lee,H. and Pedersen,L.G. A smooth
619 particle mesh Ewald method. *J. Chem. Phys.*, 1995; 103(19):8577–8593.
620 <https://doi.org/10.1063/1.470117>
- 621 32. Miyamoto, S.; Kollman, P. SETTLE: An analytical version of the SHAKE and RATTLE
622 algorithm for rigid water models. *J Comput Chem.* 1992; 13(8):952–962.
623 <https://doi.org/10.1002/jcc.540130805>
624

- 625 33. Maier JA, Martinez C, Kasavajhala K, Wickstrom L, Hauser KE, Simmerling C. ff14SB:
626 Improving the Accuracy of Protein Side Chain and Backbone Parameters from ff99SB. J
627 Chem Theory Comput. 2015; 11(8):3696-3713.
628 <https://doi.org/10.1021/acs.jctc.5b00255> PMID: [26574453](https://pubmed.ncbi.nlm.nih.gov/26574453/)
- 629 34. Ponder JW, Case DA. Force fields for protein simulations. Adv Protein Chem. 2003;
630 66:27-85. [https://doi.org/10.1016/S0065-3233\(03\)66002-X](https://doi.org/10.1016/S0065-3233(03)66002-X) PMID: [14631816](https://pubmed.ncbi.nlm.nih.gov/14631816/)
- 631 35. Lemons, Don S. Paul Langevin's 1908 paper "On the Theory of Brownian Motion" ["Sur
632 la the?orie du mouvement brownien," C. R. Acad. Sci. (Paris) 146, 530–533 (1908). Am J
633 Phys. 1997; 65(11):1079-1081. <https://doi.org/10.1119/1.18725>
- 634 36. Humphrey, W.; Dalke, A.; Schulten, K. VMD—Visual molecular dynamics. J Mol Graphics.
635 1996; 14, 33–38. [https://doi.org/10.1016/0263-7855\(96\)00018-5](https://doi.org/10.1016/0263-7855(96)00018-5)
- 636 37. Amadei A, Linssen AB, Berendsen HJ. Essential dynamics of proteins. Proteins. 1993;
637 17(4):412-425. <https://doi.org/10.1002/prot.340170408> PMID: [8108382](https://pubmed.ncbi.nlm.nih.gov/8108382/)
- 638 38. Chen J , Wang J , Xu B , et al. Insight into mechanism of small molecule inhibitors of the
639 MDM2–p53 interaction: Molecular dynamics simulation and free energy analysis. J Mol
640 Graph Model, 2011; 30:46-53. <https://doi.org/10.1016/j.jmgm.2011.06.003> PMID:
641 [21764342](https://pubmed.ncbi.nlm.nih.gov/21764342/)
- 642

Extracellular N-Terminus



Intracellular C-Terminus

Fig1

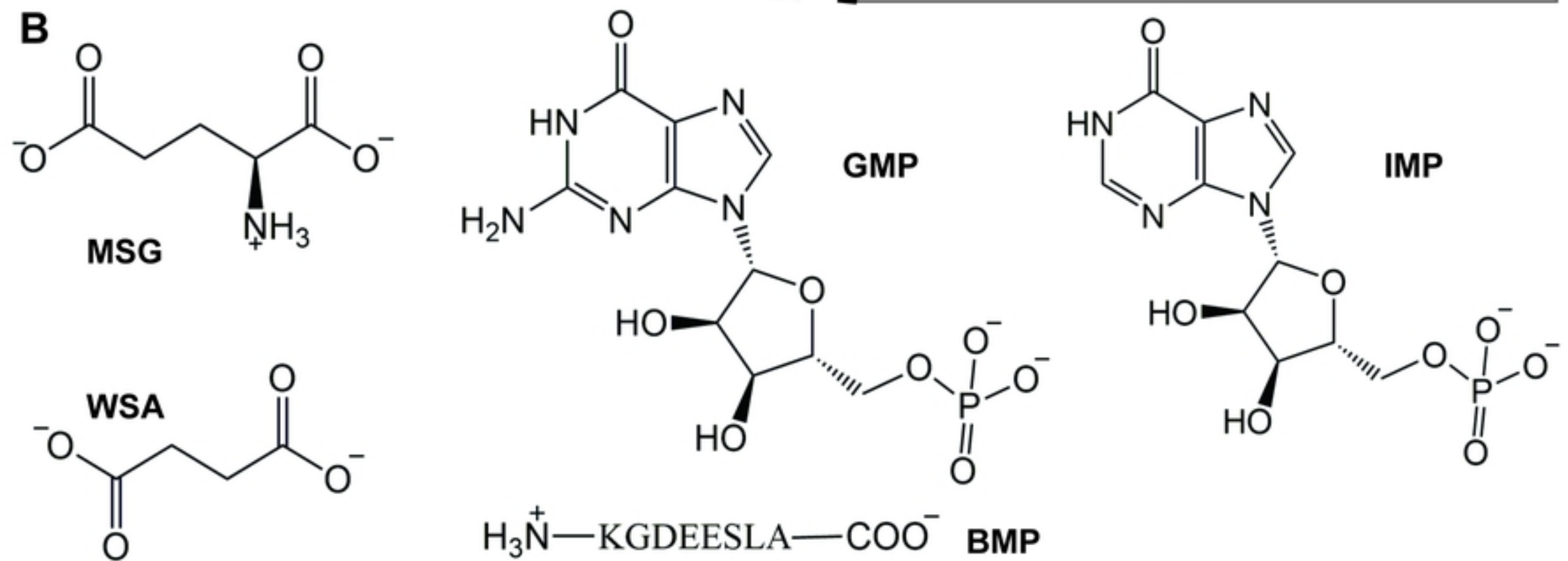
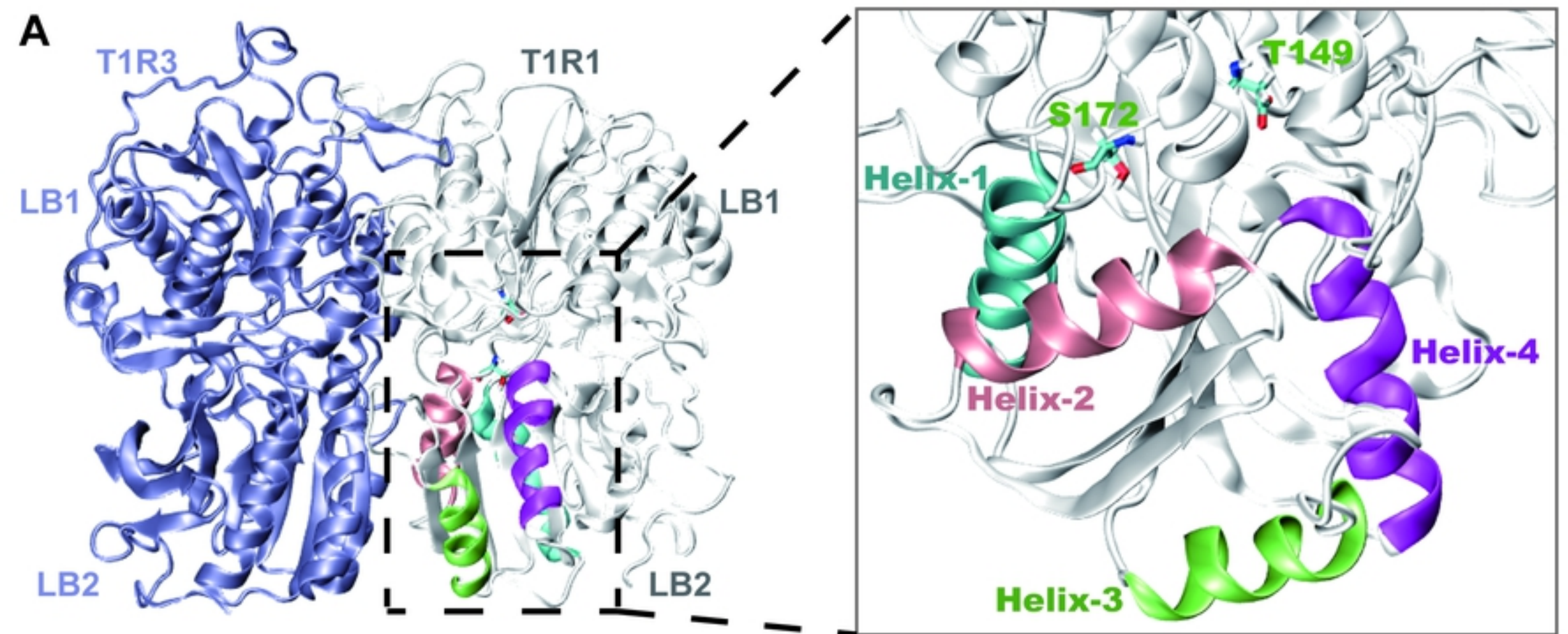


Fig2

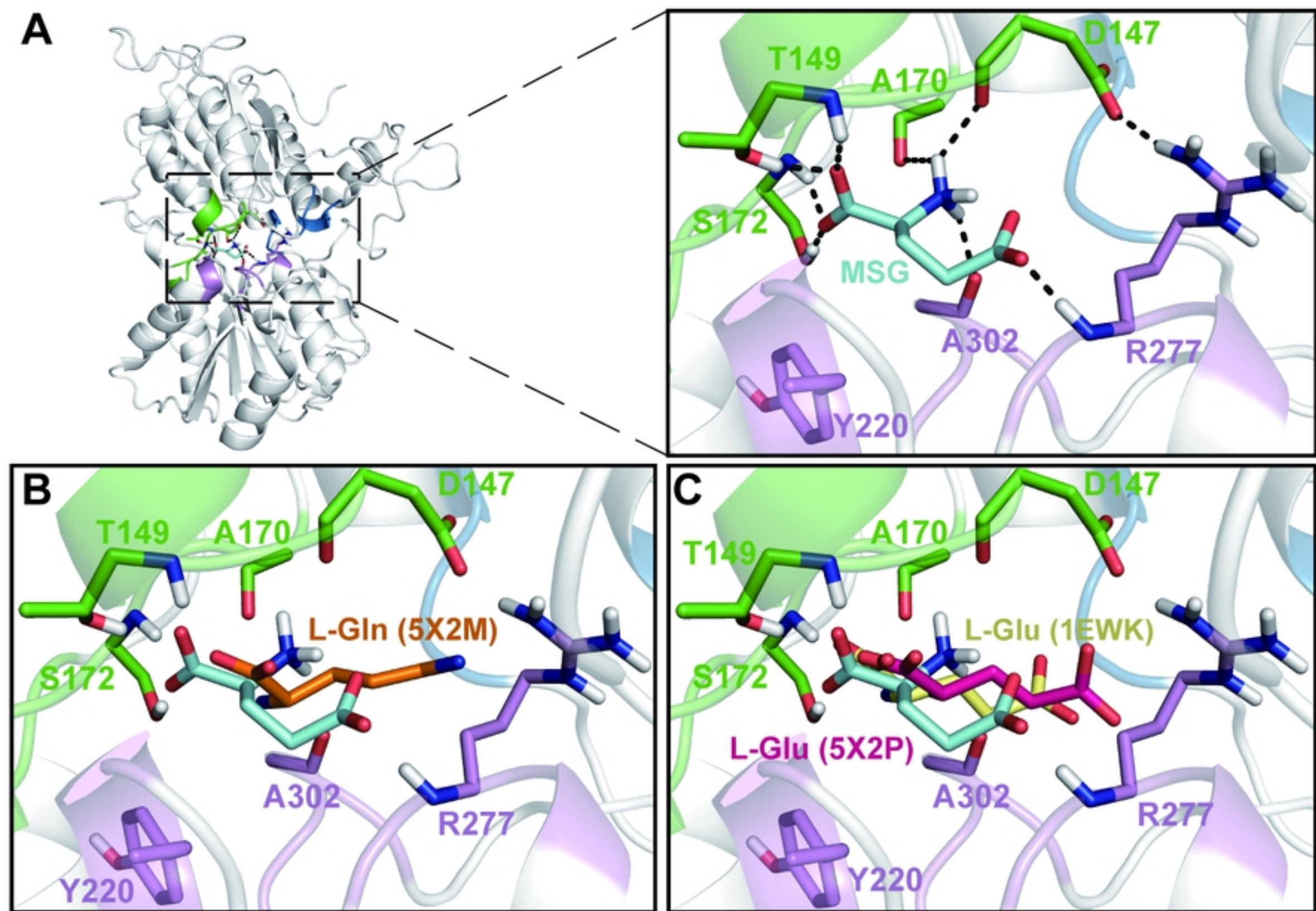


Fig3

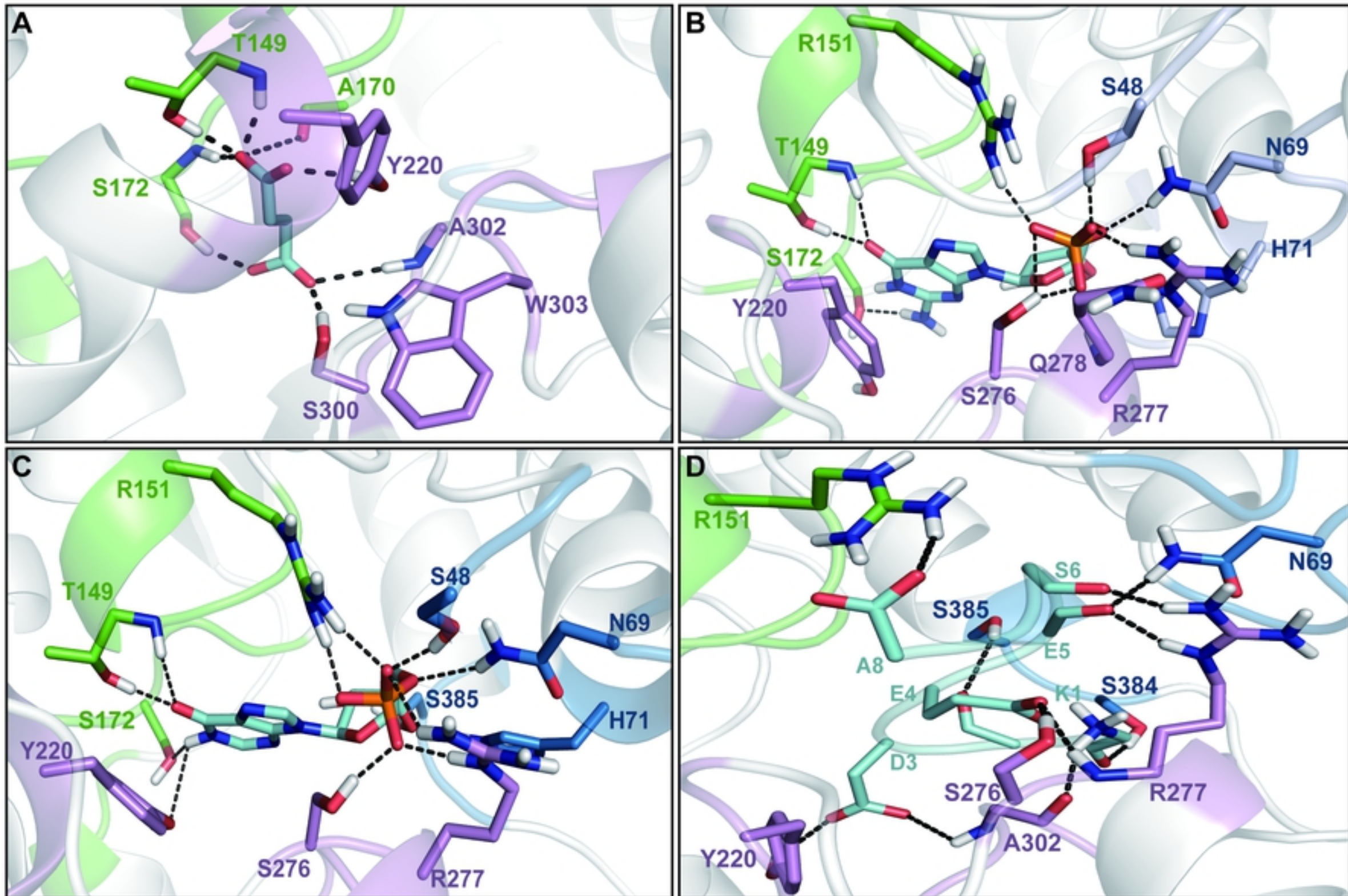


Fig4

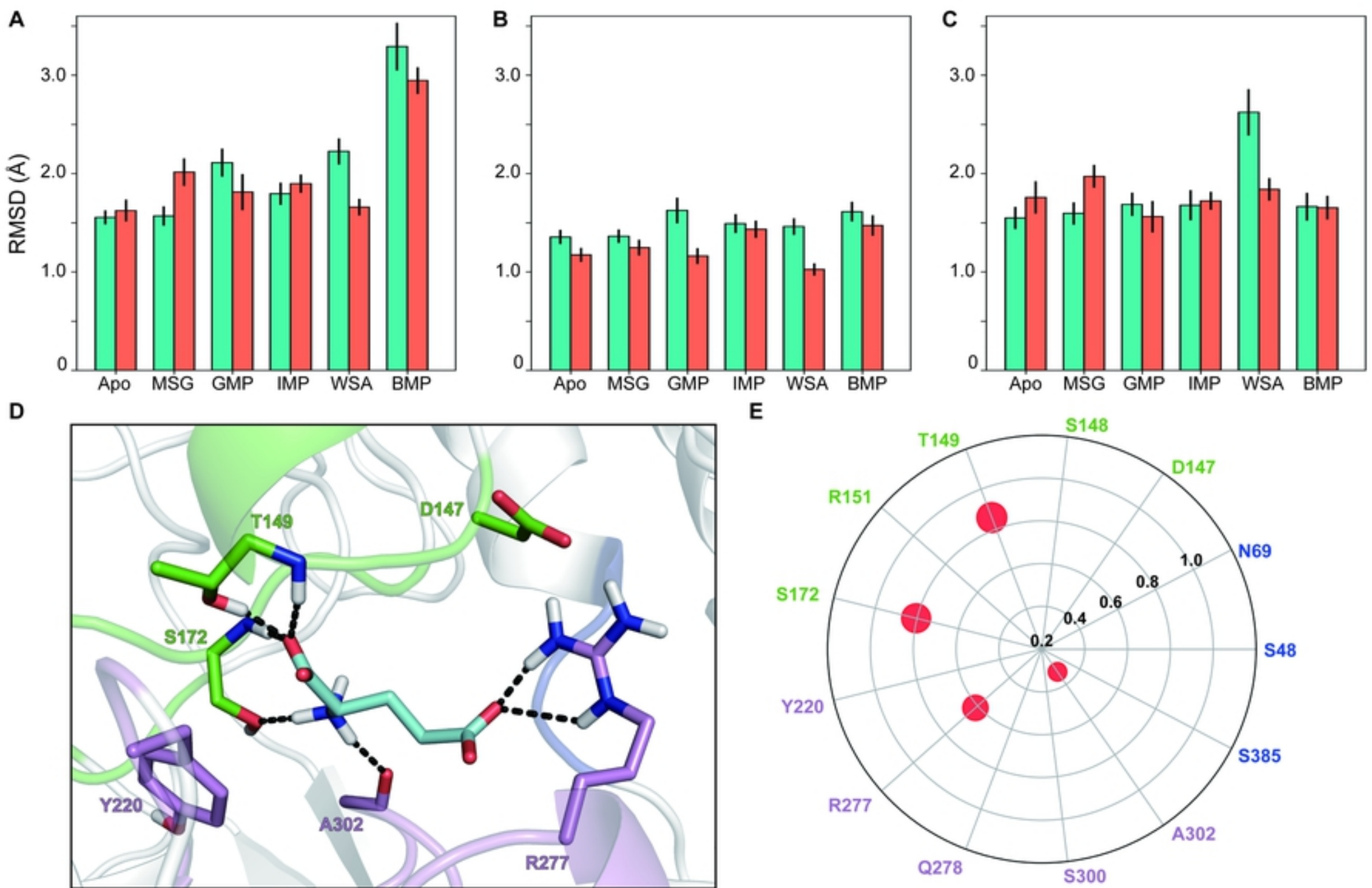


Fig5

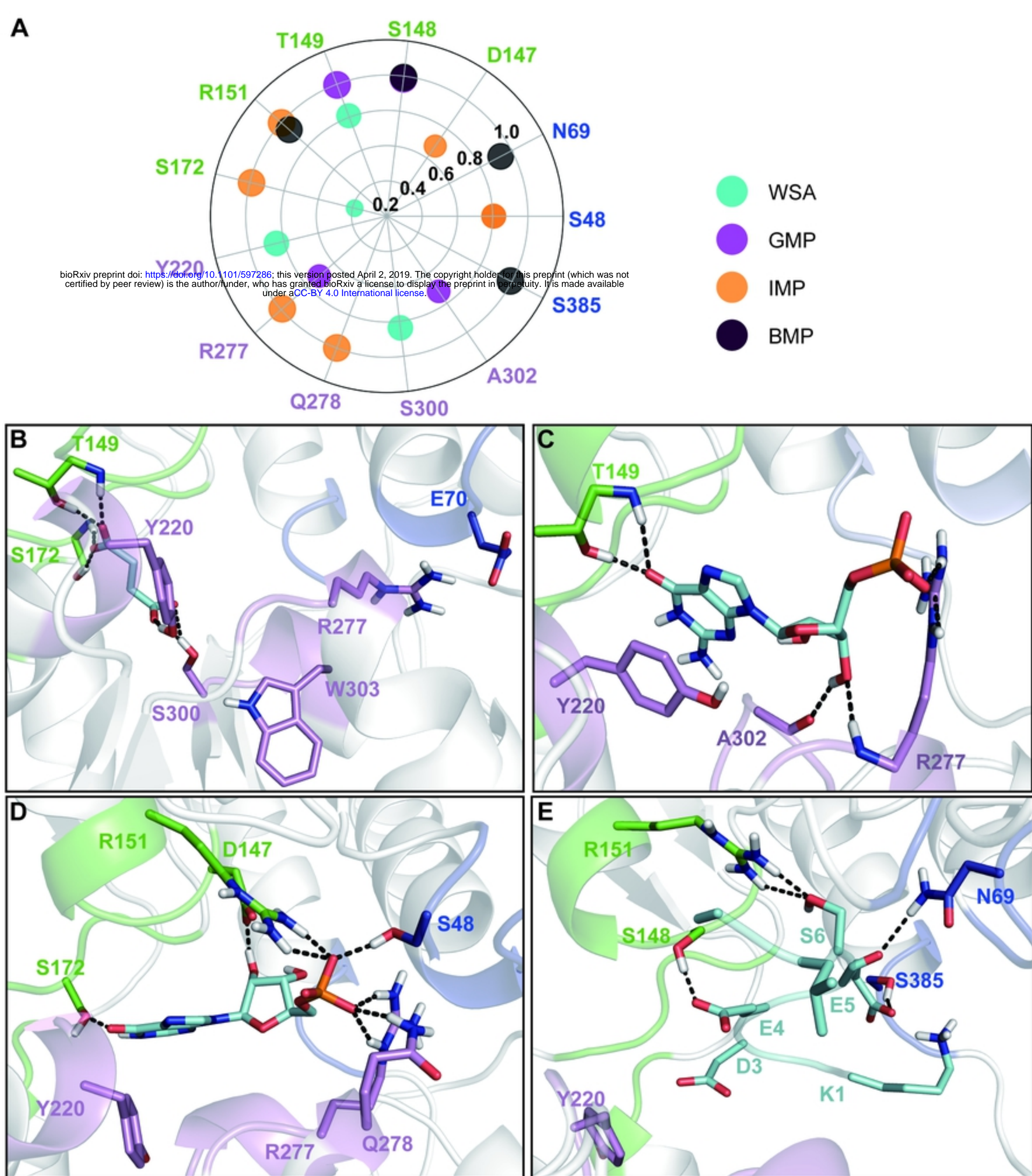


Fig6

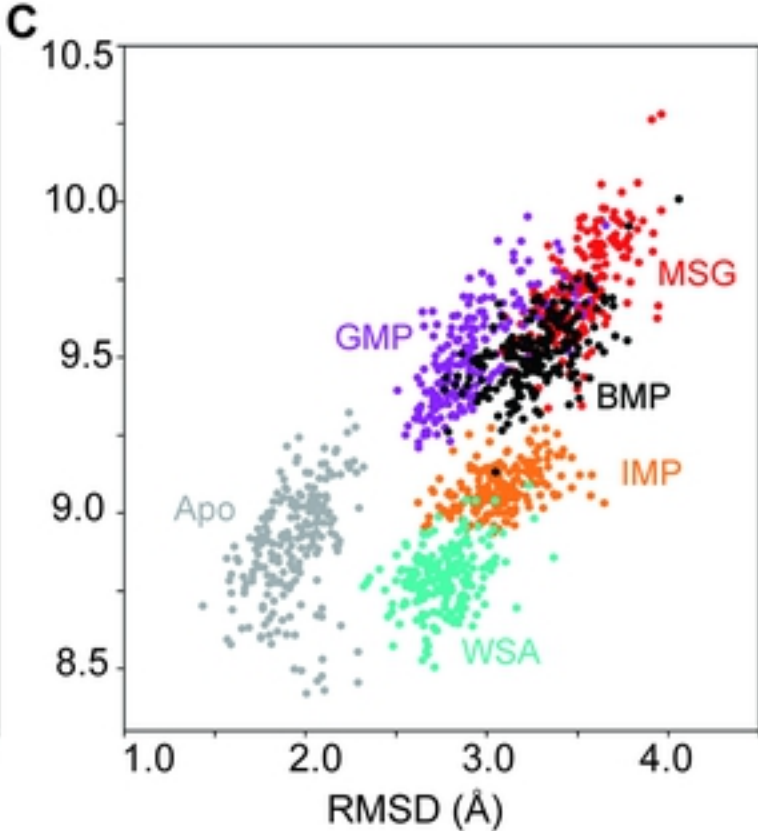
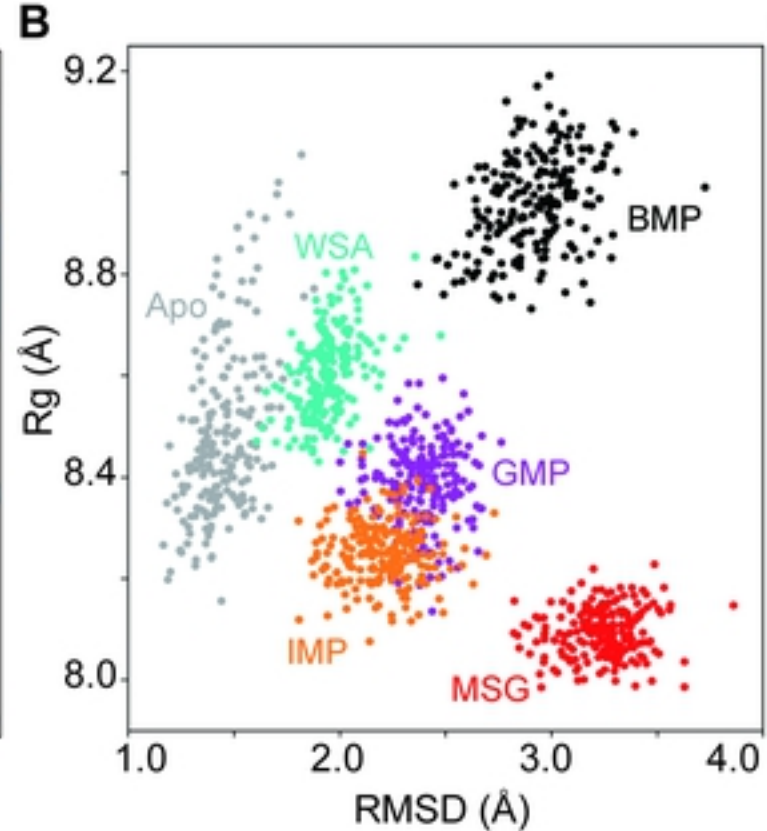
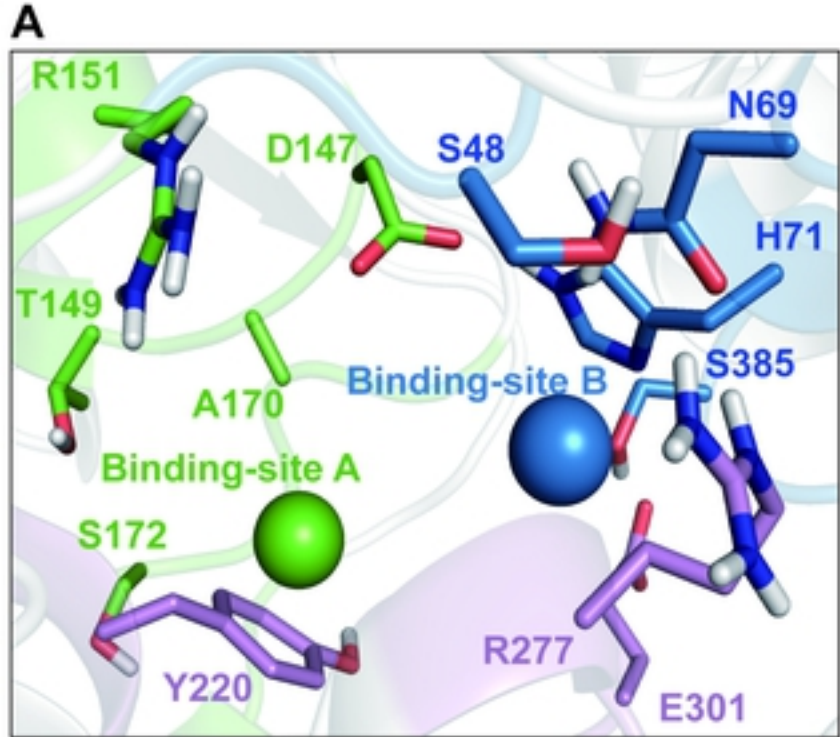


Fig7

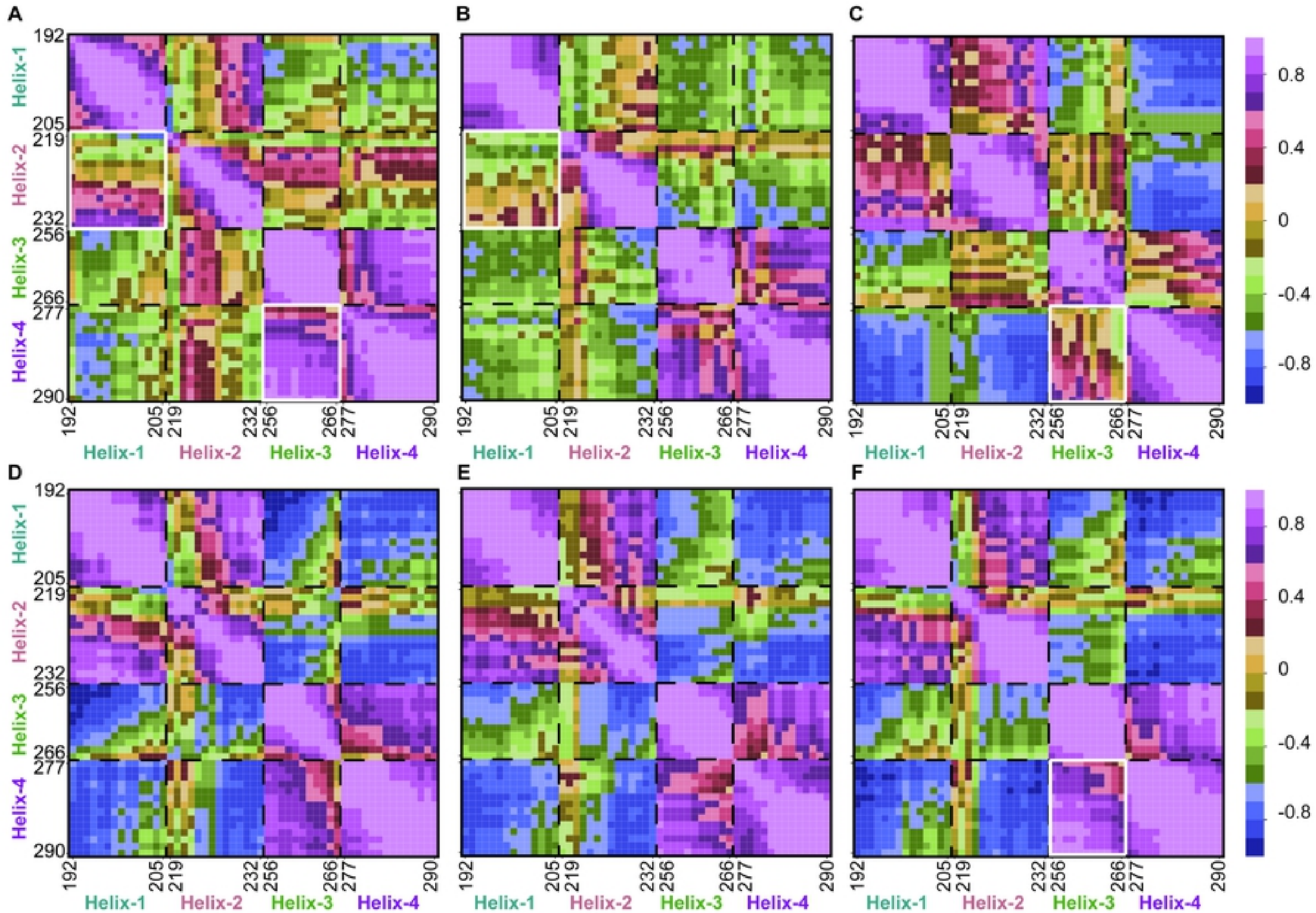
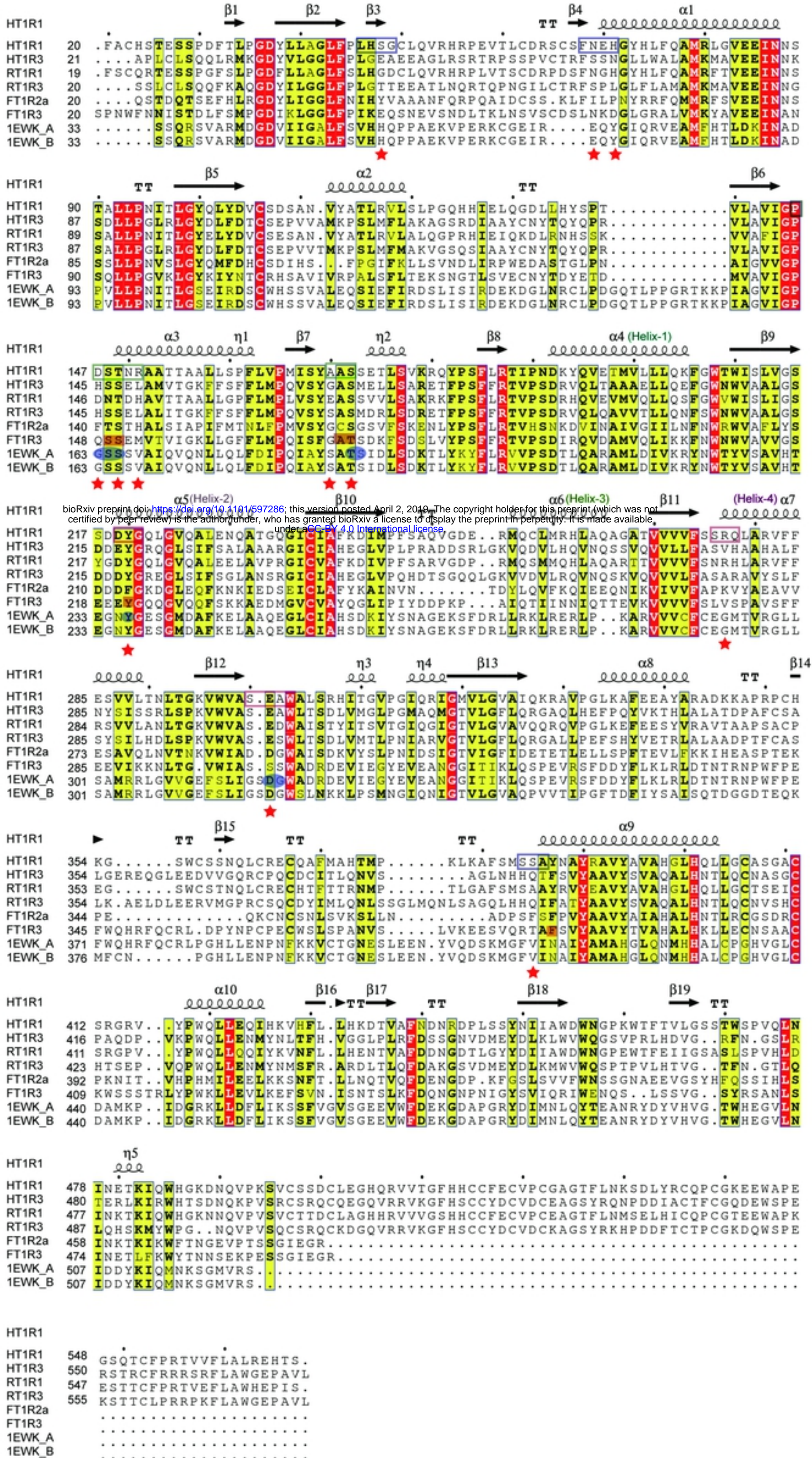
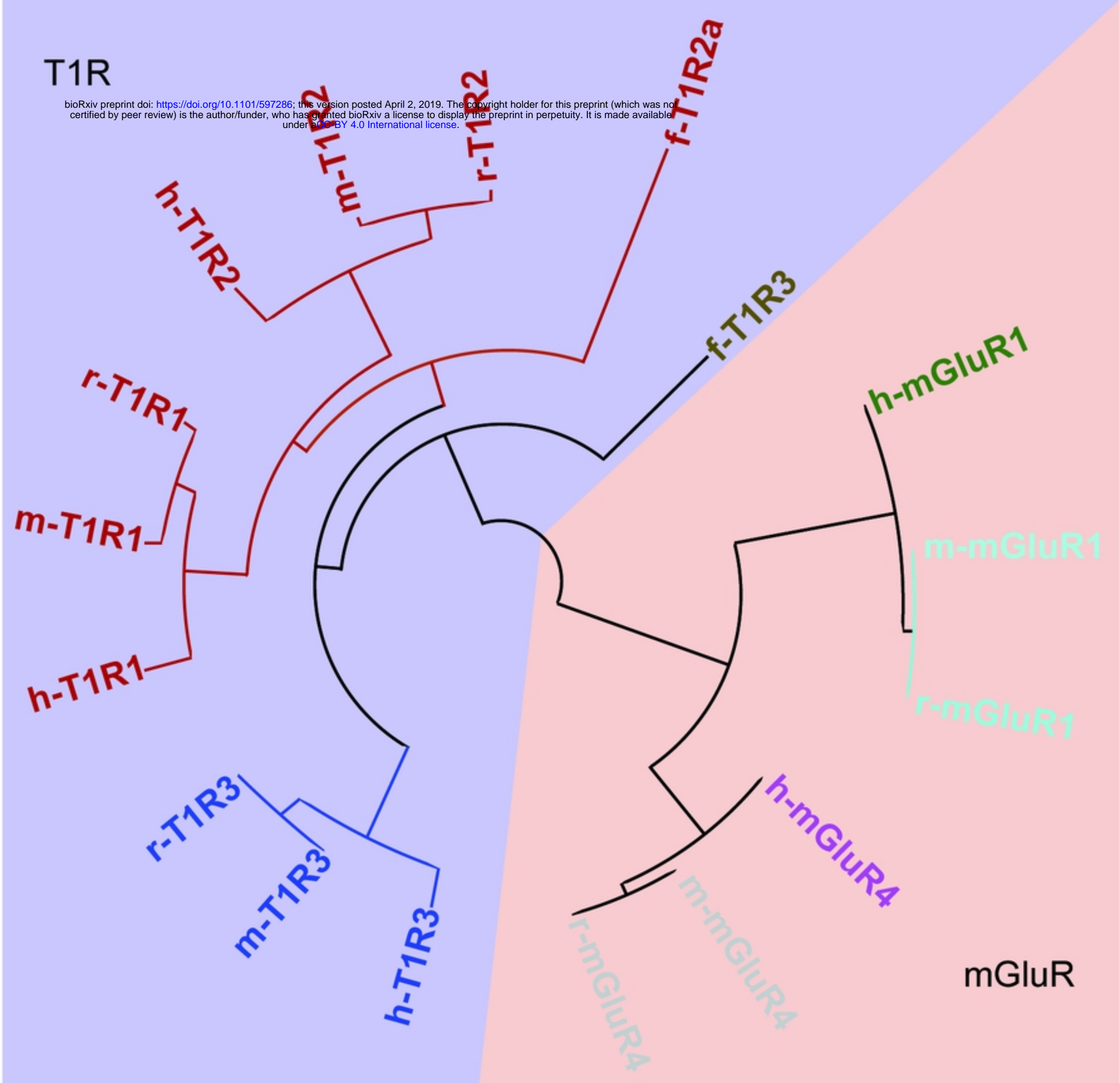


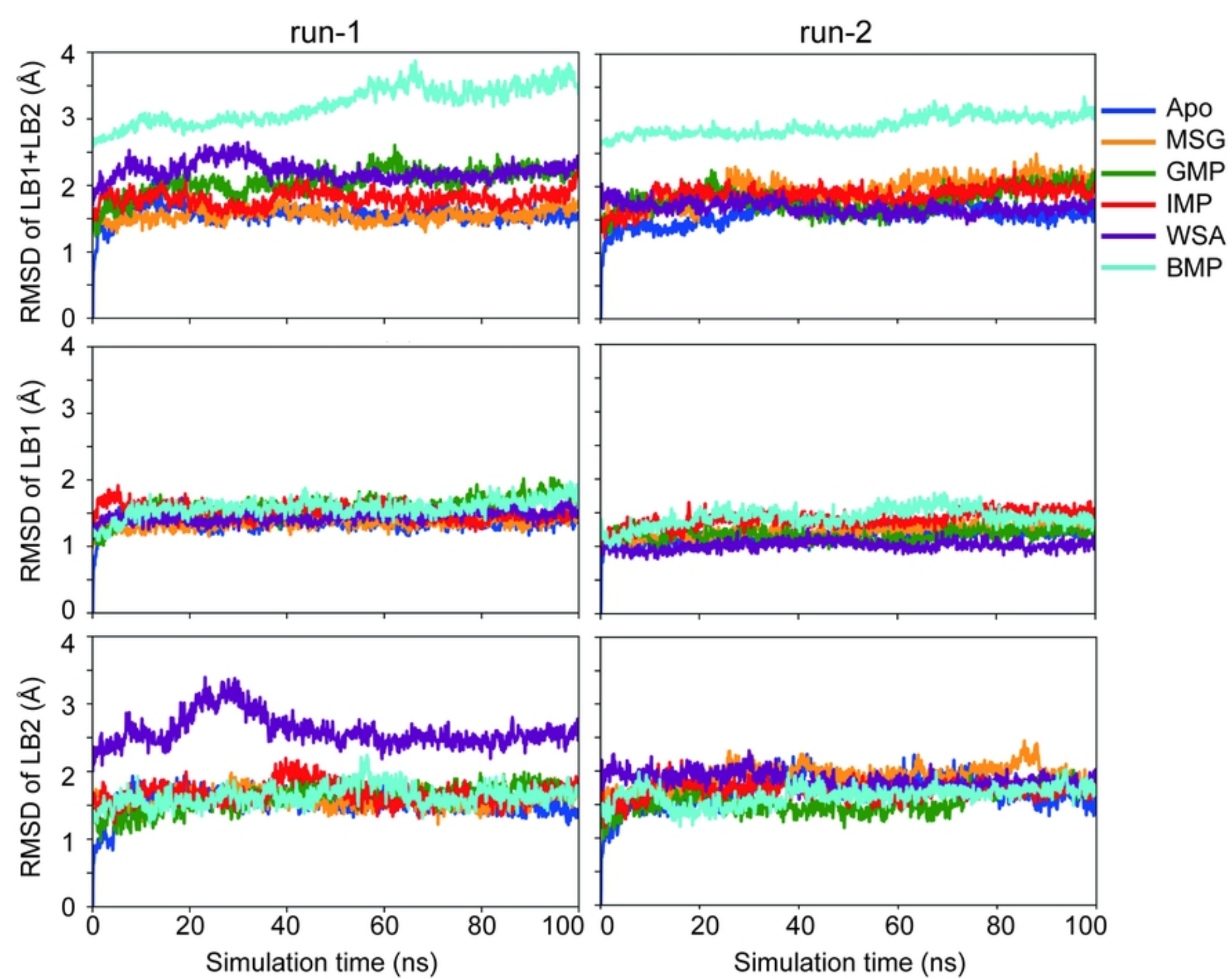
Fig8

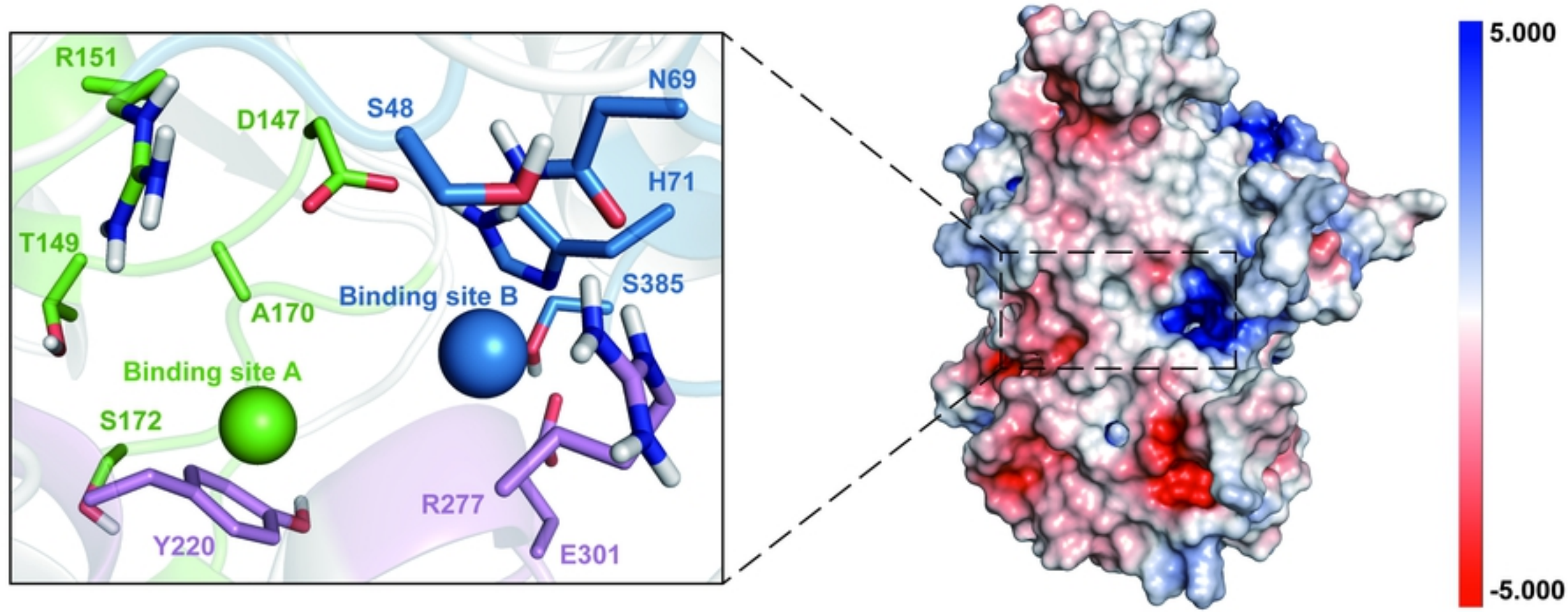


T1R

bioRxiv preprint doi: <https://doi.org/10.1101/597286>; this version posted April 2, 2019. The copyright holder for this preprint (which was not certified by peer review) is the author/funder, who has granted bioRxiv a license to display the preprint in perpetuity. It is made available under aCC-BY 4.0 International license.







S4